

Numerical study of ductile failure under non-proportional loading ¹

David Morin^{a,b}, Lars Edvard Blystad Dæhli^a, Tore Børvik^{a,b}, Ahmed Benallal^c, Odd Sture Hopperstad^{a,b,*}

^a*Structural Impact Laboratory (SIMLab), Department of Structural Engineering, Norwegian University of Science and Technology (NTNU), NO-7491 Trondheim, Norway*

^b*Centre for Advanced Structural Analysis (CASA), NTNU, NO-7491 Trondheim, Norway*

^c*Laboratoire de Mecanique et Technologie, ENS Cachan/CNRS/Universite Paris-Saclay, Cachan, France*

Abstract

This paper investigates two numerical methods for predicting the initiation of ductile failure under moderately and strongly non-proportional loading paths. Two distinct phenomena are considered as indicators for the initiation of ductile failure: (i) the localization of deformation into a narrow band and (ii) the coalescence of microscopic voids. Recent experimental data in the literature from various axisymmetric tension tests on a high-strength steel are used to calibrate and validate the two methods. In the first method, which is based on the imperfection band approach, strain localization analyses are conducted using the deformation history extracted from finite element simulations of the tension tests. In the second method, axisymmetric unit cells are utilized to evaluate the onset of void coalescence using the stress history extracted from the same finite element simulations of the experiments. The various uniaxial tension tests yield different moderately and strongly non-proportional loading paths that are used to evaluate the predictive capabilities of the two methods. The numerical results are further used to discuss the similarities and differences between the two methods. Both the strain localization analyses and the coalescence analyses are found capable of predicting the initiation of failure in the experiments with good accuracy; however, the coalescence analyses are generally in closer agreement to the experiments.

Keywords: Ductile failure; Unit cell; Gurson model; Strain localization

1. Introduction

Ductile failure is a complex mechanical process that has been studied for several decades. The complexity of this phenomenon is linked to the fact that many parameters can influence the ductility of a material. Among these parameters, the stress state, represented by dimensionless parameters such as the stress triaxiality T and the Lode parameter L , has a strong effect on the overall ductility of a metal (Bao and Wierzbicki, 2004; Barsoum and Faleskog, 2007; Gruben et al., 2011; Haltom et al., 2013; Papisidero et al., 2014). In addition to the stress state, both the strain rate and the temperature influence the ductility of a material to various extents (Chen et al., 2009; Roth and Mohr, 2014; Erice et al., 2018). Dedicated material tests are usually performed

¹This article is based on a General Lecture given at the EUROMECH Solid Mechanics Conference in Bologna, 2018

*Corresponding author

Email address: odd.hopperstad@ntnu.no (Odd Sture Hopperstad)

Nomenclature

Symbols

α	Orientation of localization band
$\dot{\mathbf{q}}$	Non-uniformity rate vector
\dot{p}	Equivalent plastic strain rate
\dot{W}_d	Deformation power
\mathbf{E}	Macroscopic strain tensor
Φ	Yield function
ψ	Ratio between generalized forces
ρ	Ratio between stress components
σ_0	Initial yield stress
Σ_{eq}	Macroscopic equivalent stress
σ_{eq}	Equivalent stress
Σ_h	Macroscopic hydrostatic stress
σ_h	Hydrostatic stress
σ_M	Matrix flow stress
σ, Σ	Stress tensors
\mathbf{C}^t	Material tangent stiffness tensor
\mathbf{d}, \mathbf{D}	Rate-of-deformation tensors
\mathbf{F}	Deformation gradient tensor
\mathbf{I}	Second-order identity tensor
\mathbf{L}	Velocity gradient tensor
\mathbf{N}	Nominal stress tensor
\mathbf{n}	Unit normal vector to imperfection band
\mathbf{P}	Generalized force vector

\mathbf{R}	Rotation tensor
θ	Deviatoric angle
ε_{eq}	Equivalent strain
ζ	Notch acuity
A_n	Nucleation rate
D_{eq}	Equivalent rate-of-deformation
E, ν	Elastic coefficients
E_{eq}	Macroscopic equivalent strain
f	Void volume fraction
f_0	Initial void volume fraction
f_g	Void volume fraction due to growth
f_n	Void volume fraction due to nucleation
f_n^{\max}	Maximum value of f_n
f_p	Particle volume fraction
L	Lode parameter
l_i, L_i	Current and reference unit cell size
p	Accumulated plastic strain
Q_i, θ_i	Isotropic hardening parameters
q_i	Tvergaard parameters
T	Stress triaxiality

Abbreviations

FE	Finite element
MPC	Multi-point constraint

to investigate the effect of these parameters on ductile failure (Gruben et al. (2012), Lou and Yoon (2017)). While material tests are important in order to study the effect of a given parameter on ductile failure, realistic loading conditions at the structural level always incorporate some degree of non-proportionality. Strongly non-proportional loading paths can for instance be found in plastically formed automotive components subjected to impact loads, but also in material tests due to the formation of a diffuse or local neck. While the effects of non-proportional loading, or strain-path change, on work hardening (Tarigopula et al., 2009; Manik et al., 2015; Wen et al., 2015; Liao et al., 2017) and formability (Vysochinskiy et al., 2018) have been investigated thoroughly in the literature within the metal forming community, the impact of such loading conditions on ductile failure is less documented.

As summarized by Thomas et al. (2016), previously published experimental studies have been focused on strongly non-proportional loading including abrupt changes in stress triaxiality. These particular loading path changes are often obtained by pre-straining a material specimen in a first phase and then re-machining the deformed specimen to change the stress state in the second phase of the test. For instance, a change in stress triaxiality is obtained by sharpening an existing notch or machining a notch on a pre-strained smooth tensile test specimen. Basu and Benzerga (2015) considered different jumps in the stress triaxiality ratio by pre-straining smooth tensile specimens and machining out notches of different acuity, which leads to an increased stress triaxiality ratio in the second phase of the tests. For a detailed overview of the previously published experimental studies dealing with similar types of loading, the reader is referred to Thomas et al. (2016). It was recently shown by Papisidero et al. (2015) that the effect of pre-straining on ductile failure can also be investigated using tubular specimens subjected to combined compression/tension or tension/torsion loadings. A general trend found in these studies is that the failure strain is strongly dependent upon the loading path and that local stress state variations can lead to increased or decreased ductility. In an attempt to overcome this difficulty, efforts have been devoted to develop experimental procedures to control the local stress state of material test samples. Roth and Mohr (2015) showed that a nearly proportional stress state can be obtained using advanced test setups. The drawbacks of such setups are that a limited number of stress states can be investigated and that the tests may not be suitable for all materials.

With the recent increase in computational power, numerical methods have become increasingly popular for ductile failure assessments. In contrast to experiments, numerical models offer the opportunity to investigate ductile failure with full control of the boundary conditions, which alleviates some of the issues associated with experimental testing. However, one important limitation of numerical analyses compared to experiments is that the instant of failure is not a natural outcome of the simulations and must be defined appropriately. Moreover, the obtained results may be highly dependent upon the choice of constitutive model and discretization. This was demonstrated by Dæhli et al. (2017) using 3D unit cell analyses. Their results show that changing the definition of the localization indicator leads to large variations in both the shape of the failure locus and the magnitude of the failure strain of an idealized material. Therefore, special care must be taken within a numerical framework to obtain consistent results.

Consistency in numerical analyses can be obtained by considering a specific state or event in the ductile failure process. As illustrated in Figure 1, ductile failure of porous polycrystalline solids ① starts by diffuse plastic flow ②, which is accompanied by growth of existing voids and nucleation of new voids. After some deformation, strain localization occurs ③ due to some kind of material instability and the plastic flow localizes ④ while void growth outside the localization band stops. It is worth mentioning that strain localization can be the result of local material heterogeneities or imperfections, but could also be the result of a geometrical constraint. Within the zone of localized deformation, accelerated void growth takes place until neighbouring voids start to interact, which defines the onset of coalescence ⑤. Ductile failure results from the formation of a macro-crack due to coalescence of several microscopic voids ⑥.

Unit cell analyses have become a common way of investigating ductile failure. By using such a numerical framework, the loading state applied to a representative volume element is fully defined and particular microstructural features, such as the shape and distribution of voids or particles, can be studied. Ductile failure is usually assumed to correspond to the onset of coalescence (i.e., ⑤ in Figure 1) in the unit cell modelling framework. Unit cell analyses have been used in several numerical studies on the effect of non-proportional loading over the past ten years. Vadillo and Fernández-Sáez (2009) imposed various stress triaxiality paths to an axisymmetric unit cell model to calibrate a Gurson model with the q_i parameters given as functions of the stress triaxiality ratio. Zhang and Skallerud (2010) studied the combined effects of pre-straining and void shape on ductile failure using axisymmetric unit cells. Benzerga et al. (2012)

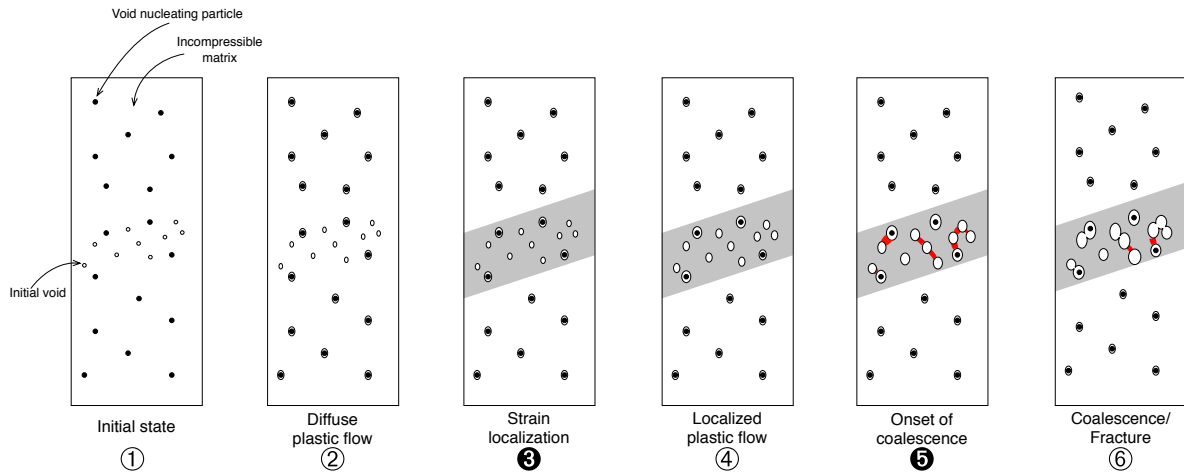


Figure 1: Ductile failure process in a material consisting of an incompressible matrix with particles and pre-existing voids.

used a similar framework, based on axisymmetric unit cells, to study the differences between a failure locus obtained under radial and non-radial loadings. Yu et al. (2016) extended the two previous studies by conducting both axisymmetric and 3D unit cell analyses under proportional and non-proportional loading. By using 3D unit cell analyses, Yu et al. (2016) were also able to investigate the effect of non-proportional loading in terms of the Lode parameter. These numerical studies showed a good qualitative agreement with previous experimental observations made in the literature. Dæhli et al. (2016) investigated the influence of the loading path on ductile fracture of aluminium alloys using 2D axisymmetric unit cells. Both proportional and non-proportional loading paths were applied and the predicted failure strains were compared qualitatively and quantitatively for several aluminium alloys. In that study, instead of using generic and presumed stress states, the authors used a set of numerical simulations of the tensile tests conducted on these alloys by Westermann et al. (2014) to extract the evolution of the stress triaxiality. This approach gave promising quantitative estimates of the ductility of the studied aluminium alloys.

With reference to Figure 1, if ductile failure is the result of void coalescence and the formation of a macro-crack, strain localization phenomena (③ in Figure 1) are usually strong indicators for imminent failure. Strain localization phenomena have been thoroughly investigated from a numerical point of view. Marciniak and Kuczyński (1967) proposed to use the existence of a non-uniformity to explain localized necking in thin sheets subjected to biaxial tension. This approach has been widely used to investigate the ductility of metallic materials in the sense of local necking (see for instance the work of Pedersen et al. (2008)). A similar numerical approach to study strain localization is the imperfection band analysis framework proposed by Rice (1976). This framework allows to evaluate the emergence of strain localization into an imperfection band in a more general 3D context, as opposed to the approach proposed by Marciniak and Kuczyński (1967), which is limited to plane stress situations. The imperfection band approach has been applied in various context by Yamamoto (1978), Needleman and Rice (1978), Saje et al. (1982), Pan et al. (1983), Mear and Hutchinson (1985), Needleman and Tvergaard (1992), Nahshon and Hutchinson (2008), Xue et al. (2013), Dæhli et al. (2017), Morin et al. (2018b), and Dæhli et al. (2018). These studies demonstrate that the imperfection band analyses are capable of describing the same trends as observed in experiments, such as the effect of the stress state on ductile failure. Recently, Gruben et al. (2017) and Morin et al. (2018a) employed imperfection band analyses to quantitatively predict the ductility of two advanced high strength steels and a

high strength aluminium alloy, respectively. In those studies, ductile failure was assumed to initiate when the strain rate becomes infinite inside the imperfection band. The imperfection band was governed by the porous plasticity model proposed by Gurson (1977), while the material outside the band was assumed to be perfectly sound and therefore modelled using metal plasticity. To drive the strain localization analyses, the stress state obtained by finite element (FE) analyses of the material test was applied to the material outside the band. This approach gave promising quantitative results in the referenced studies for tensile-dominated deformation modes with moderate non-proportionality.

In this study, both strain localization analyses based on the imperfection band approach and unit cell analyses are used to predict the initiation of ductile failure. The aim is to assess the accuracy of the two methods for moderately and strongly non-proportional loading paths. To this end, the experimental data reported by Basu and Benzerga (2015) are used to calibrate and evaluate the two simulation methods.

The paper is organized as follows. Section 2 describes the numerical methods along with their respective advantages and disadvantages. Section 3 summarizes the experimental work of Basu and Benzerga (2015). The calibration of the unit cell and strain localization analyses is treated in Section 4. Section 5 describes the numerical results and the assessment of the two approaches. Section 6 provides a discussion of the results, while concluding remarks are given in Section 7.

2. Numerical methods

2.1. Overview

The two methods applied in this study are conceptually described in Figure 2 a) and b), illustrating the strain localization analyses and the unit cell analyses, respectively. A single uniaxial tension test is applied to calibrate the metal plasticity model (① in Figure 2 a)), which is further used to represent the matrix material in the unit cell analyses and the material outside the band in the strain localization analyses. An initial set of unit cell analyses conducted under proportional loading is used to calibrate the porous plasticity model (② in Figure 2 a)) that governs the material inside the imperfection band of the strain localization analyses. To determine appropriate material parameters for the imperfection in the strain localization analyses, the deformation history obtained from the simulation of the uniaxial tension test with the calibrated metal plasticity model is assigned to the material outside the imperfection band (③ in Figure 2 a)). Using this deformation history, the relevant material parameter of the imperfection is adjusted until a good agreement is found between the experimental failure strain and the predicted value.

As for the strain localization analyses, the metal plasticity model used to describe the matrix material in the unit cell analyses is identified based on a uniaxial tension test. Following Dæhli et al. (2016), the stress history in the uniaxial tension test is extracted from a numerical simulation and used to drive the unit cell analyses (① in Figure 2 b)). The volume fraction of the initial void or the particle is adjusted until we obtain agreement between the onset of coalescence in the unit cell analyses and failure in the experiment. In the remaining sections of this article, when a unit cell analysis is subjected to the stress history of a numerical simulation to predict failure, the term coalescence analysis is employed. The term unit cell analysis is limited to the analyses required to calibrate the porous plasticity model used in the imperfection analyses.

2.2. Stress state parameters

In this section, we define the stress state parameters that are referred to throughout this work. We note that the macroscopic stress tensor (Σ) is used in this presentation, but the stress state parameters presented below also apply to the microscopic (or local) stress tensor (σ).

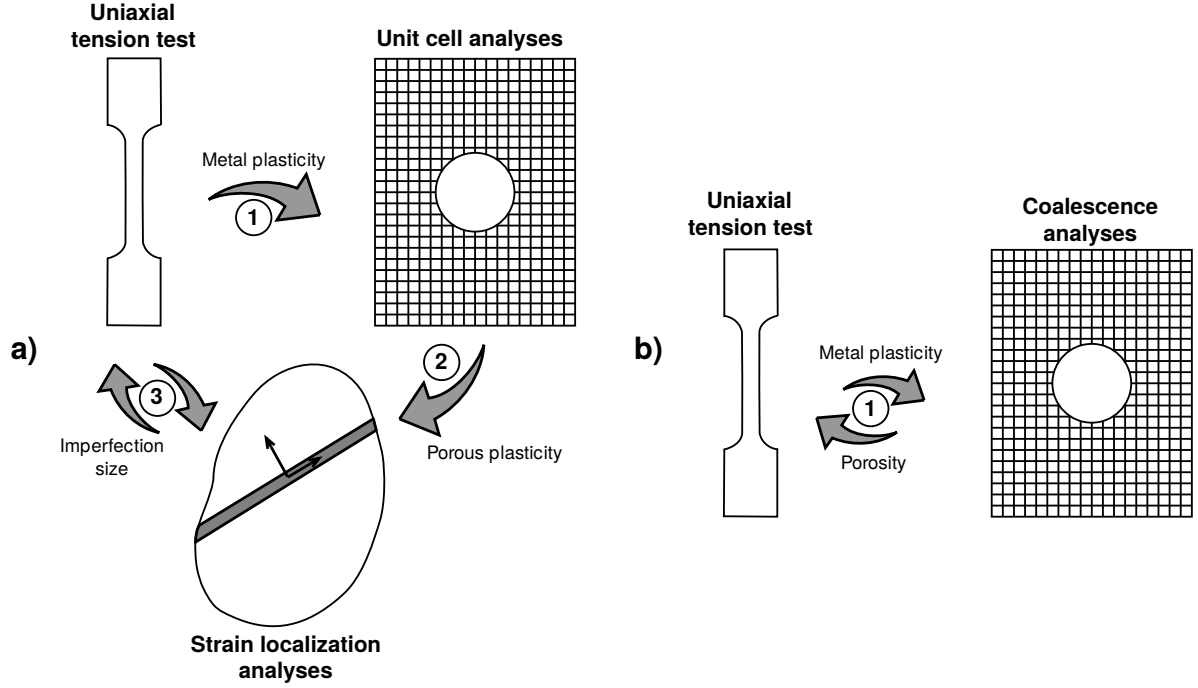


Figure 2: Description of the proposed approaches: a) strain localization analyses and b) coalescence analyses with unit cells.

An arbitrary stress state, denoted P in Figure 3, can be expressed in the principal stress space with the principal stress components written as the sum of a deviatoric part (Σ') and a hydrostatic part (Σ_h), viz.

$$\Sigma_1 = \Sigma'_1 + \Sigma_h = \frac{2}{3}\Sigma_{eq} \cos(\theta) + \Sigma_h \quad (1a)$$

$$\Sigma_2 = \Sigma'_2 + \Sigma_h = \frac{2}{3}\Sigma_{eq} \cos\left(\theta - \frac{2\pi}{3}\right) + \Sigma_h \quad (1b)$$

$$\Sigma_3 = \Sigma'_3 + \Sigma_h = \frac{2}{3}\Sigma_{eq} \cos\left(\theta + \frac{2\pi}{3}\right) + \Sigma_h \quad (1c)$$

where θ is the deviatoric angle, $\Sigma_{eq} = \sqrt{3J_2}$ is the von Mises equivalent stress, and $\Sigma_h = I_1/3$ is the hydrostatic stress. Here, the second principal deviatoric stress invariant and the first principal stress invariant are denoted J_2 and I_1 , respectively. In this work, we make use of the isotropic properties of the material such that the deviatoric angle is confined to lie within the range $\theta \in [0^\circ, 60^\circ]$. The stress components are then ordered according to $\Sigma_1 \geq \Sigma_2 \geq \Sigma_3$. We refer to Figure 3a for an illustration of the stress state P in the principal stress space and to Figure 3b for a corresponding illustration in the deviatoric stress plane. Note that the deviatoric angle (θ) is the angle between the direction of the stress point (P) and a projected base vector (\mathbf{m}_1) along the Σ_1 -axis in the deviatoric plane.

In the following, we will use the stress triaxiality T and the Lode parameter L to describe the stress state. These will also be used in conjunction with the unit cell analyses to prescribe given macroscopic loading histories. To this end, the stress triaxiality is defined from the hydrostatic stress Σ_h and the von Mises

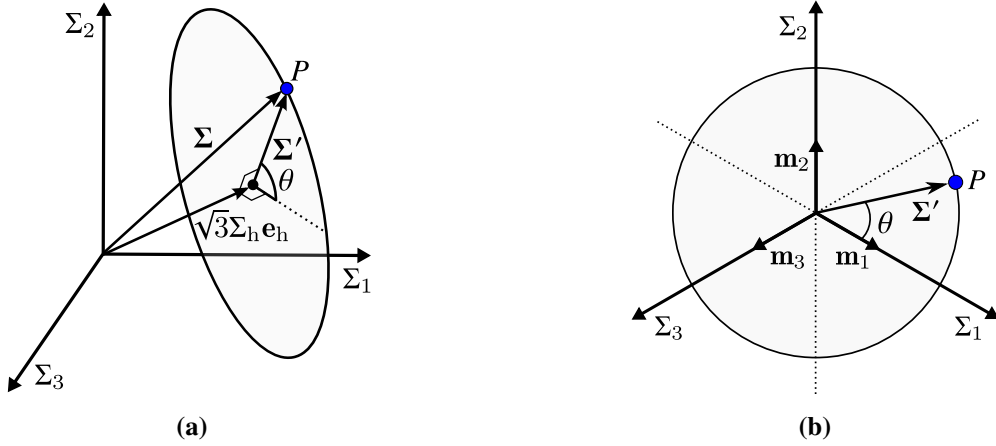


Figure 3: Illustration of a stress point P in (a) the principal stress space and (b) the deviatoric stress plane. The deviatoric and hydrostatic parts of the stress vector are indicated in the figure and the hydrostatic axis is denoted by \mathbf{e}_h . The depicted ellipse, which is a circle in the deviatoric plane, describes stress points with the same hydrostatic stress level Σ_h .

equivalent stress Σ_{eq} as

$$T = \frac{\Sigma_h}{\Sigma_{\text{eq}}} \quad (2)$$

The Lode parameter describes the deviatoric stress state and is defined as a ratio between the principal stress components, viz.

$$L = \sqrt{3} \tan\left(\theta - \frac{\pi}{6}\right) = \frac{2\Sigma_2 - \Sigma_1 - \Sigma_3}{\Sigma_1 - \Sigma_3} \quad (3)$$

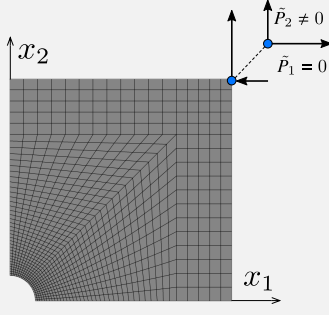
From the definition of the Lode parameter, it follows that $L = -1$ and $L = +1$ correspond to $\theta = 0^\circ$ and $\theta = 60^\circ$, respectively. These two stress states in turn describe states of generalized tension ($\Sigma_1 \geq \Sigma_2 = \Sigma_3$) and generalized compression ($\Sigma_1 = \Sigma_2 \geq \Sigma_3$). These types of stress states are associated with axisymmetric specimens with different notch acuity that are loaded in tension or compression, respectively. In this study, we will predominantly impose stress states corresponding to $L = -1$ in the unit cell analyses. However, stress states defined by $L = +1$ are employed in Section 6.3 to highlight some difficulties associated with evaluating the onset of void coalescence in the unit cell simulations for generalized compression and the effect of the Lode parameter on the resulting prediction of ductile failure.

2.3. Unit cell analyses

In this study, we employ 2D axisymmetric unit cell analyses to evaluate the onset of coalescence, which is used as an indicator for material failure. The finite element mesh is shown in Box 1, where approximately 1000 fully integrated linear axisymmetric elements are used to discretize the matrix material. Two types of unit cell analyses are used in this study: (i) a unit cell with an initial void or (ii) a unit cell with an embedded particle. Both the void and the particle are assumed to be initially spherical. In the case of the unit cell analyses with a particle, a friction-less interface with hard contact in the normal direction is employed to model the interaction between the particle and the matrix material. While the shape of the particle and the cohesion energy of the particle-matrix interface are assumed to be important (Dæhli et al., 2016), we disregard these effects in the current study. This is partly motivated by the lack of experimental data for the cohesive properties of this interface and partly by the desire to limit the complexity of the numerical analyses.

The finite element analyses are conducted using the implicit ABAQUS/Standard solver (Dassault Systèmes Simulia, 2014) with the default direct sparse solver and the non-linear geometry option activated.

Box 1: Overview of the setup for the unit cell analyses (Dæhli et al., 2016).

<ul style="list-style-type: none"> • Macroscopic stress and strain rate vectors $\{\Sigma\}, \{\mathbf{D}\}$ (4) • Macroscopic equivalent stress $\Sigma_{\text{eq}} = \Sigma_{22} - \Sigma_{11}$ (5) • Macroscopic strain (no sum on i) $E_{ii} = \ln\left(\frac{l_i}{L_i}\right)$ (6) • Macroscopic equivalent strain $E_{\text{eq}} = \frac{2}{3} E_{22} - E_{11}$ (7) • Total deformation power $\dot{W}_d = V\{\Sigma\}^T\{\mathbf{D}\}$ $= V(2\Sigma_{11}D_{11} + \Sigma_{22}D_{22})$ (8) • Stress triaxiality $T = \frac{\Sigma_h}{\Sigma_{\text{eq}}} = \frac{2\Sigma_{11} + \Sigma_{22}}{3 \Sigma_{22} - \Sigma_{11} }$ (9) 		<ul style="list-style-type: none"> • Ratio between stress components $\rho = \frac{\Sigma_{11}}{\Sigma_{22}} = \frac{3T - 1}{3T + 2}$ (10) • Generalized forces $\{\mathbf{P}\} = V\{\Sigma\} = \begin{Bmatrix} P_1 \\ P_2 \end{Bmatrix}$ (11) • Ratio between generalized forces $\psi = \frac{P_1}{P_2} = 2\rho$ (12) • Power-equivalent dummy node $\dot{W}_d = \{\mathbf{P}\}^T\{\mathbf{D}\} = \{\tilde{\mathbf{P}}\}^T\{\tilde{\mathbf{D}}\}$ (13) • Transformation of generalized force and strain rate vectors $\{\mathbf{P}\} = [\mathbf{Q}]\{\tilde{\mathbf{P}}\} \quad \wedge \quad \{\mathbf{D}\} = [\mathbf{Q}]\{\tilde{\mathbf{D}}\}$ (14) • Orthogonal transformation matrix $[\mathbf{Q}] = \frac{1}{\sqrt{1 + \psi^2}} \begin{bmatrix} 1 & \psi \\ -\psi & 1 \end{bmatrix}$ (15)
--	---	---

The metal plasticity model compiled in Box 2 governs the matrix material in the unit cell analyses and consists of a regular J_2 plasticity model (see Dæhli et al. (2017) and Morin et al. (2018a)). To account for the yield plateau exhibited by the investigated material, a modified Voce rule is used to describe the isotropic work hardening. As indicated in Equation (21), work hardening is triggered when the equivalent plastic strain p reaches a threshold p_0 . The particle, when present, is represented by a linear elastic material. We employ a multi-point constraint (MPC) subroutine (Dassault Systèmes Simulia, 2014) to control the stress state imposed to the unit cell in a similar way as described by Faleskog et al. (1998) and Cheng and Guo (2007). A brief summary of the main equations governing the MPC subroutine and the macroscopic stress and strain measures for the unit cell is given in Box 1 and we refer the reader to Dæhli et al. (2016) for a more detailed overview of this procedure.

In this study, we use the onset of coalescence as an indicator for the initiation of ductile failure in the unit cell analyses. The onset of coalescence is associated with a shift in the response to a uniaxial straining mode, with subsequent plastic deformation confined to the intervoid ligament (Koplik and Needleman, 1988; Benzerga et al., 2012). Figure 4 shows results from a unit cell analysis of the considered material carried out under a constant stress triaxiality of $T = 1$ and a constant Lode parameter of $L = -1$. Figure 4 a) describes the evolution of the macroscopic equivalent stress and the void volume fraction as a function of the macroscopic equivalent strain (see Box 1 for definitions). Figure 4 b) represents the deformed shape of the unit cell and the field map of the equivalent plastic strain rate \dot{p} for two different levels of strain. The onset of softening ❶ in the unit cell is characterized by the maximum equivalent stress in Figure 4 a). At this loading stage, the matrix material of the unit cell still undergoes plastic flow ($\dot{p} > 0$) apart from a small zone at the apex of the void (Figure 4 b)). The onset of coalescence corresponds to the knee in the evolution of the void volume fraction (indicated by ❷ in Figure 4 a)). This occurs when the deformation localizes in the intervoid

Box 2: Overview of the metal plasticity model (Dæhli et al., 2017).

<ul style="list-style-type: none"> • Corotational formulation 	$\hat{\sigma} = \mathbf{R}^T \cdot \sigma \cdot \mathbf{R} \quad \wedge \quad \hat{\mathbf{d}} = \mathbf{R}^T \cdot \mathbf{d} \cdot \mathbf{R} \quad (16)$	<ul style="list-style-type: none"> • Isotropic work hardening 	$\sigma_M = \sigma_0 + \sum_{i=1}^3 Q_i \left(1 - \exp \left(-\frac{\theta_i}{Q_i} (p - p_0) \right) \right) \quad (21)$
<ul style="list-style-type: none"> • Additive decomposition of strain rate 	$\hat{\mathbf{d}} = \hat{\mathbf{d}}^e + \hat{\mathbf{d}}^p \quad (17)$	<ul style="list-style-type: none"> • Associated flow rule 	$\hat{\mathbf{d}}^p = \lambda \frac{\partial \Phi}{\partial \hat{\sigma}} \quad (22)$
<ul style="list-style-type: none"> • Generalized Hooke's law on rate form 	$\hat{\sigma} = \frac{E}{1+\nu} \hat{\mathbf{d}}^e + \frac{E}{3(1-2\nu)} \text{tr}(\hat{\mathbf{d}}^e) \mathbf{I} \quad (18)$	<ul style="list-style-type: none"> • Equivalent plastic strain 	$p = \int_0^t \dot{p} d\bar{t} = \int_0^t \lambda d\bar{t} \quad (23)$
<ul style="list-style-type: none"> • Yield function 	$\Phi(\hat{\sigma}, p) = \sigma_{\text{eq}}(\hat{\sigma}) - \sigma_M(p) \leq 0 \quad (19)$	<ul style="list-style-type: none"> • Loading-unloading conditions 	$\Phi \leq 0, \quad \lambda \geq 0, \quad \lambda \Phi = 0 \quad (24)$
<ul style="list-style-type: none"> • Equivalent stress 	$\sigma_{\text{eq}}(\hat{\sigma}) = \sqrt{\frac{3}{2} \hat{\sigma}' : \hat{\sigma}'} \quad (20)$		

ligament (see Figure 4 b)), while unloading ($\dot{p} = 0$) takes place in the other regions of the unit cell.

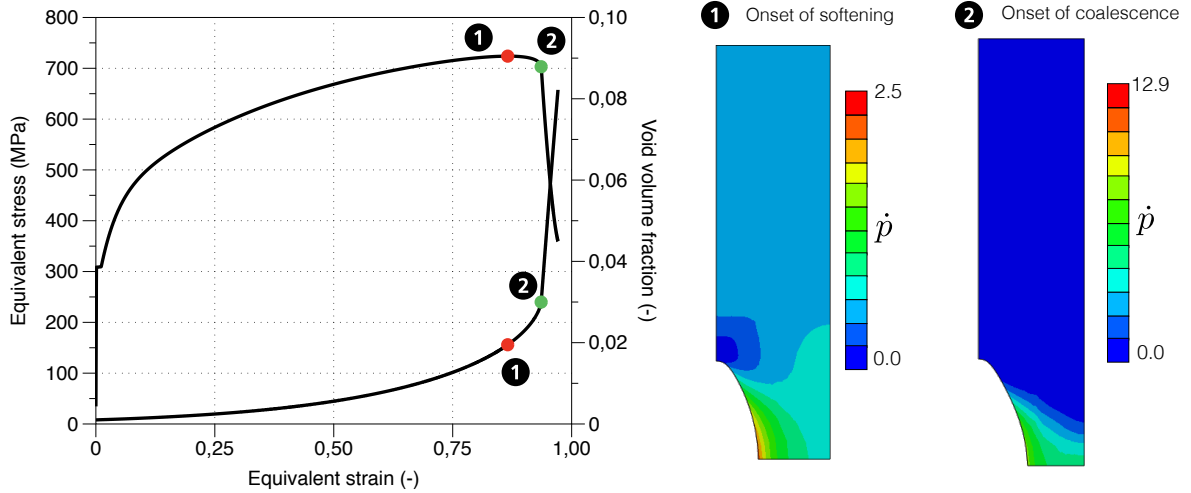


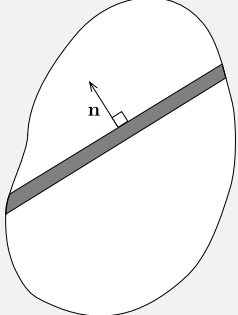
Figure 4: Results of a unit cell analysis of the investigated material.

2.4. Strain localization analyses

The imperfection band approach proposed by Rice (1976) considers a homogeneous material, apart from an embedded thin planar imperfection band, subjected to an overall homogeneous deformation. In this work, we will use such an approach to conduct strain localization analyses. While this method does not impose any restrictions on the constitutive equations of the material inside the imperfection band or on the material outside this band, we will follow the same approach as in Nahshon and Hutchinson (2008), Gruben et al. (2017), and Morin et al. (2018a) in the current study. We consequently assume that any voiding mechanism taking place in the material outside the band is negligible and the metal plasticity model compiled in Box 2 is used to represent this material. This assumption is usually appropriate for rather low stress triaxialities, as illustrated for instance by Xue et al. (2010, 2013) and Westermann et al. (2014). A brief overview of the

governing equations of the imperfection band approach is given in Box 3. The reader is referred to Rice (1976), Needleman and Rice (1978), and Morin et al. (2018b) for more comprehensive treatments.

Box 3: Overview of the strain localization analyses (Morin et al., 2018b).

<ul style="list-style-type: none"> • Continuing equilibrium $\mathbf{n} \cdot \dot{\mathbf{N}}_b = \mathbf{n} \cdot \dot{\mathbf{N}}_o \quad (25)$ • Constitutive equations outside the band $\dot{\mathbf{N}}_o = \mathbf{C}_o^t : \mathbf{L}_o \quad (26)$ • Constitutive equations inside the band $\dot{\mathbf{N}}_b = \mathbf{C}_b^t : \mathbf{L}_b \quad (27)$ • Compatibility $\mathbf{L}_b = \mathbf{L}_o + \dot{\boldsymbol{\epsilon}} \otimes \mathbf{n} \quad (28)$ 		<ul style="list-style-type: none"> • Equation system for the non-uniformity rate vector $\dot{\boldsymbol{\epsilon}}$ $(\mathbf{n} \cdot \mathbf{C}_b^t \cdot \mathbf{n}) \cdot \dot{\boldsymbol{\epsilon}} = \mathbf{n} \cdot (\mathbf{C}_o^t - \mathbf{C}_b^t) : \mathbf{L}_o \quad (29)$ • Band orientation in updated configuration $\mathbf{n} = \begin{bmatrix} \cos \alpha \\ 0 \\ \sin \alpha \end{bmatrix} \quad (30)$ • Localization conditions $\det(\mathbf{n} \cdot \mathbf{C}_b^t \cdot \mathbf{n}) = 0 \quad (31)$ $\xi = \sqrt{\frac{\mathbf{D}_b : \mathbf{D}_b}{\mathbf{D}_o : \mathbf{D}_o}} \rightarrow \infty \quad (32)$
---	---	---

We use a porous plasticity model to represent the material of the imperfection band. This type of model offers a rather simple way to introduce an imperfection in the form of either pre-existing voids or void nucleation. An overview of the porous plasticity model used in this study is given in Box 4. The use of a porous plasticity model inside the imperfection band allows to introduce material softening, which triggers loss of ellipticity of the governing equations. As shown by Rudnicki and Rice (1975), material softening is required for loss of ellipticity to occur when an associated flow rule is adopted. It is worth mentioning that any kind of constitutive equation can be used inside the imperfection band. However, models that do not incorporate material softening will not trigger loss of ellipticity (for associated plastic flow), but might produce an exponential growth of the deformation inside the imperfection band. This is similar to the approach proposed by Marciniak and Kuczyński (1967). In the present study, two types of imperfections are investigated: (i) the imperfection band is considered as an initially voided material with initial void volume fraction f_0 or (ii) the imperfection band is considered to be free of pre-existing voids ($f_0 = 0$), but consists of particles from which voids nucleate ($\dot{f}_n \geq 0$). Instead of the nucleation rule proposed by Chu and Needleman (1980), we assume in the following that the nucleation process is uniform with respect to the equivalent plastic strain p until a maximum volume fraction of nucleated voids f_n^{\max} has been reached (see Box 4). The main incentive for this nucleation rule is its simplicity. Nucleation is governed by the nucleation rate A_n , which determines the rate at which the maximum volume fraction f_n^{\max} is reached. Recent experimental investigations based on tomography imaging show that in a dual-phase steel, void nucleation occurs continuously during the deformation process (Landron et al., 2011; Balan et al., 2015).

To illustrate how the strain localization analyses work, we show the results from an analysis conducted at constant stress triaxiality T and Lode parameter L in Figure 5 (here $T = 1$ and $L = -1$). The imperfection band is characterized by an initial void volume fraction of $f_0 = 0.005$. Figure 5 a) shows the evolution of the von Mises equivalent stress inside and outside the imperfection band, in addition to the evolution of the void volume fraction inside the band as a function of the equivalent plastic strain outside the band (p_o). We observe that as the deformation proceeds, the void volume fraction inside the band increases and results in material softening, which is indicated by the decrease of the von Mises equivalent stress. It is worth noting that the equivalent plastic strain inside the imperfection band (p_b) is larger than that outside the band as a

Box 4: Overview of the porous plasticity model (Dæhli et al., 2017).

<ul style="list-style-type: none"> • Corotational formulation $\dot{\hat{\Sigma}} = \mathbf{R}^T \cdot \dot{\Sigma} \cdot \mathbf{R} \quad \wedge \quad \dot{\hat{\mathbf{D}}} = \mathbf{R}^T \cdot \dot{\mathbf{D}} \cdot \mathbf{R} \quad (33)$	<ul style="list-style-type: none"> • Isotropic work hardening $\sigma_M = \sigma_0 + \sum_{i=1}^3 Q_i \left(1 - \exp\left(-\frac{\theta_i}{Q_i} \langle p - p_0 \rangle\right) \right) \quad (38)$
<ul style="list-style-type: none"> • Additive decomposition of strain rate $\dot{\hat{\mathbf{D}}} = \dot{\hat{\mathbf{D}}}^e + \dot{\hat{\mathbf{D}}}^p \quad (34)$	<ul style="list-style-type: none"> • Associated flow rule $\dot{\hat{\mathbf{D}}}^p = \lambda \frac{\partial \Phi}{\partial \hat{\Sigma}} \quad (39)$
<ul style="list-style-type: none"> • Generalized Hooke's law on rate form $\dot{\hat{\Sigma}} = \frac{E}{1+\nu} \dot{\hat{\mathbf{D}}}^e + \frac{E}{3(1-2\nu)} \text{tr}(\dot{\hat{\mathbf{D}}}^e) \mathbf{I} \quad (35)$	<ul style="list-style-type: none"> • Equivalent plastic strain $p = \int_0^t \dot{p} \, d\bar{t} = \int_0^t \frac{\hat{\Sigma} : \dot{\hat{\mathbf{D}}}^p}{(1-f)\sigma_M} \, d\bar{t} \quad (40)$
<ul style="list-style-type: none"> • Yield function $\Phi = \left(\frac{\Sigma_{\text{eq}}}{\sigma_M} \right)^2 + 2q_1 f \cosh\left(\frac{q_2}{2} \frac{\text{tr}(\hat{\Sigma})}{\sigma_M} \right) - 1 - q_3 f^2 \leq 0 \quad (36)$	<ul style="list-style-type: none"> • Evolution of void volume fraction $\dot{f} = \dot{f}_g + \dot{f}_n = (1-f) \text{tr}(\dot{\hat{\mathbf{D}}}^p) + A_n \dot{p}, \quad f_n \leq f_n^{\text{max}} \quad (41)$
<ul style="list-style-type: none"> • Equivalent stress $\Sigma_{\text{eq}}(\hat{\Sigma}) = \sqrt{\frac{3}{2} \hat{\Sigma}' : \hat{\Sigma}'} \quad (37)$	<ul style="list-style-type: none"> • Loading-unloading conditions $\Phi \leq 0, \quad \lambda \geq 0, \quad \lambda \Phi = 0 \quad (42)$

consequence of the simultaneous fulfilment of the compatibility conditions and the continuing equilibrium equations. In this particular case, we find from the simulations that at localization, the equivalent plastic strain reads $p_o = 0.75$ in the material outside the band and $p_b = 0.91$ inside the imperfection band. Figure 5 b) illustrates two important quantities within a strain localization analysis plotted as a function of the equivalent plastic strain outside the band; namely the determinant of the acoustic tensor in the imperfection band material $\det(\mathbf{n} \cdot \mathbf{C}_b^t \cdot \mathbf{n})$ and ξ , the ratio between the norms of the strain rate inside and outside the band. Figure 5 b) shows that as the material outside the imperfection band is deformed, the determinant of the acoustic tensor $\det(\mathbf{n} \cdot \mathbf{C}_b^t \cdot \mathbf{n})$ is decreasing slowly towards zero, while the ratio ξ is rather close to unity up to an equivalent plastic strain of approximately $p_o = 0.7$. After that, the straining accelerates inside the imperfection band and strain localization occurs. While the stringent condition for strain localization is defined by the determinant of the acoustic tensor being identically equal to zero (Box 3), this value is not attained exactly in numerical analyses. Instead, the first negative value of the determinant is used as localization indicator. Although this difference might influence the predictions seen from inside the imperfection band due to the high strain rate in the vicinity of localization (see the evolution of ξ in Figure 5 b)), it is completely negligible with respect to the quantities outside the band. Accordingly, using either zero determinant of the acoustic tensor or attainment of a critical ratio ξ as an indicator for ductile failure has a negligible effect on the quantities of the material outside the band.

3. Review of the experimental results

This section gives a brief description of the experimental study of Basu and Benzerga (2015), including two series of tensile tests respectively with and without strain path change. The experimental work was motivated by a previous theoretical study on the effect of loading path on the fracture locus of ductile materials (Benzerga et al., 2012).

The investigated material was taken from a thick cold-rolled medium-carbon A572 Grade-50 steel plate, which has a ferritic-pearlitic microstructure with a 25 μm average grain size. According to Basu and Benzerga (2015), this material was chosen for two reasons: (i) the damage mechanisms are well known and consist of

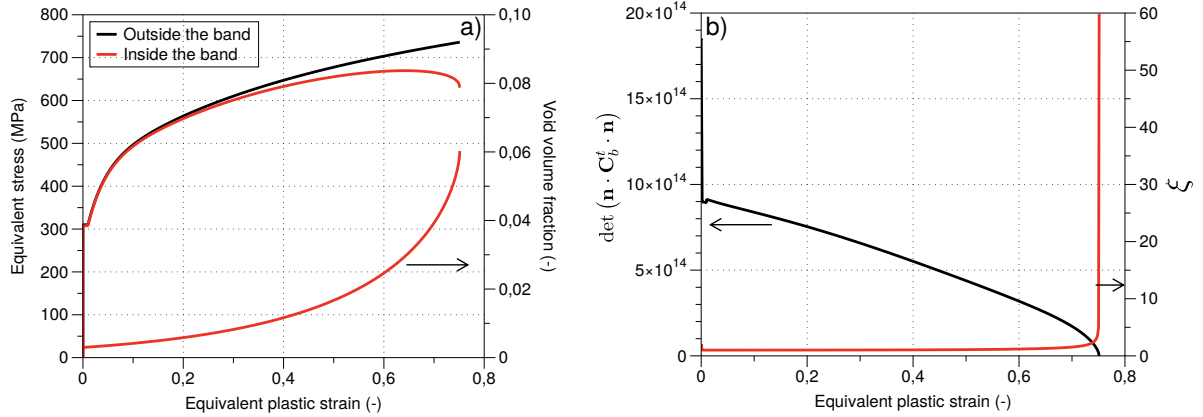


Figure 5: Results of a strain localization analysis in terms of a) equivalent stress and void volume fraction and b) the determinant of the acoustic tensor and the strain rate ratio ξ as a function of the equivalent plastic strain outside the imperfection band.

nucleation at rather small strains around sulfides or oxides (Benzerga et al., 2004), and (ii) plastic anisotropy can be neglected (Benzerga et al., 2004).

The experimental programme was based on round axisymmetric bars with or without notches. A first series of tests was conducted on the virgin material and referred to as experiments without path change. These experiments included a smooth tensile specimen and three types of notched specimens with different notch acuity ζ . An illustration showing the diameter of the specimens and a definition of the notch acuity ζ are given in Figure 6 a). Three different notch acuity values were employed, corresponding to $\zeta = 9.3, 4.6,$ and 1.5 (Basu and Benzerga, 2015), which led to different average stress triaxiality ratios of approximately $T = 0.8, 1.0,$ and $1.4,$ respectively. These experiments will be referred to as monotonic experiments in the following.

The second part of their experimental programme was dedicated to non-proportional loading conditions. This series of tests was referred to as experiments with path change. The test protocol was as follows (this process is shown schematically in Figure 6 b)):

- Four large diameter smooth tensile bars ① were deformed until incipient necking ② and then unloaded.
- A notch of desired acuity ζ was machined in the central region of each pre-deformed smooth bar ③.
- The notched specimens were deformed to failure ④ .

Four different values of notch acuity ζ were investigated, leading to four average stress triaxialities of approximately $T = 0.9, 1.2, 1.6,$ and $1.8.$ These experiments will be referred to as non-monotonic in the following.

All tests were instrumented with a load cell of capacity 110 kN to measure the load applied to the specimens. The specimen elongation was recorded using an extensometer of gauge length $L_0 = 25.4$ mm, while some experiments were instrumented with a custom-made diameter reduction measuring device. The experiments were carried out under constant cross-head velocity and the velocity was adjusted so as to keep the strain rate within the range 10^{-4}s^{-1} to $10^{-3}\text{s}^{-1}.$ It was concluded that the active damage mechanisms were not affected by the potential variations in strain rate.

Fractography using scanning electron microscopy (SEM) was carried out on the investigated specimens. These SEM fractographs (Figure 6 in Basu and Benzerga (2015)) confirmed that the ductile failure mechanism

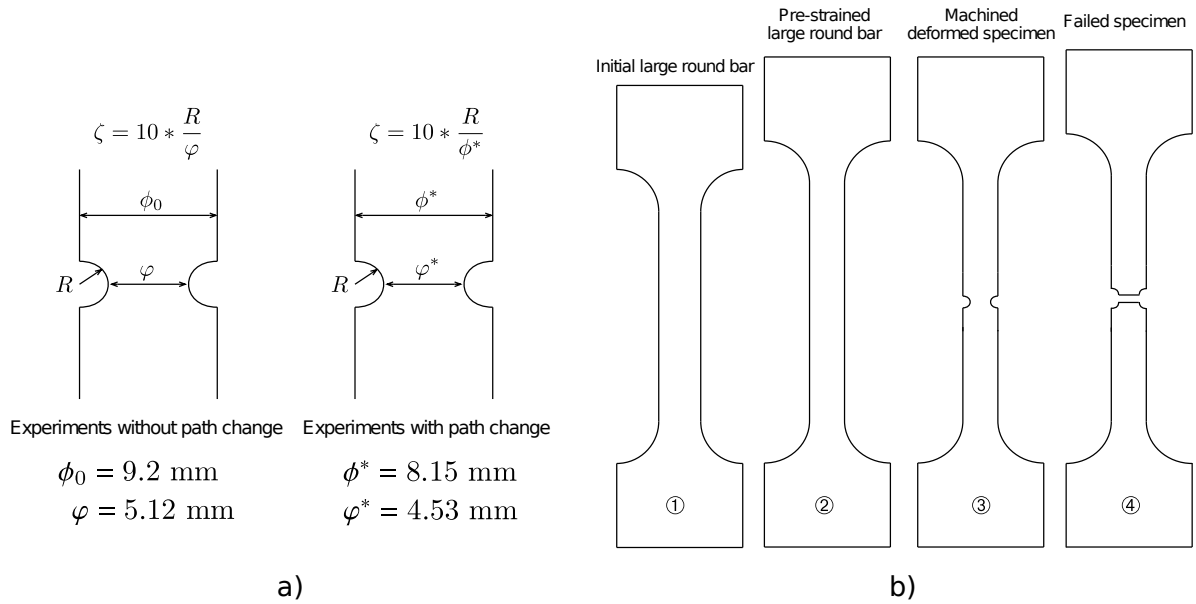


Figure 6: Description of a) the notch acuity ζ and b) the experimental protocol of the non-monotonic experiments.

was governed by the process of nucleation, growth and coalescence of voids. The hypothesis of negligible plastic anisotropy in the thick cold-rolled steel plate was also confirmed by observing that the cross-section of the different specimens remained nearly circular up to failure. Basu and Benzerga (2015) reported that no signs of surface cracking were observed in the various experiments, which suggests that failure initiated near the centre of the specimens.

4. Calibration

The two approaches for ductile failure assessment applied in this study require the calibration of several parameters. Both methods employ a constitutive model based on metal plasticity (see Figure 2 and Box 2) and we present the calibration of this model first. Next, we present the calibration of the porous plasticity model, which is further used to determine appropriate values for the initial void volume fraction or the nucleation parameter within the strain localization analyses. Lastly, the initial void volume fraction and the particle volume fraction required in the coalescence analyses with unit cells are calibrated.

4.1. Metal plasticity

The metal plasticity model assumes isotropic behaviour in both the elastic and plastic domain. As the elasticity parameters are given standard values from the literature, the calibration procedure reduces to finding suitable values for the yield stress and work-hardening parameters (see Box 2). In the following, we will use reverse engineering of the uniaxial tensile test to determine these parameters. To this end, an axisymmetric model of the tensile test is simulated using the implicit finite element solver ABAQUS/Standard (Dassault Systèmes Simulia, 2014). Linear elements with reduced integration were employed in the simulations. Owing to the symmetries of the specimen and the assumed material isotropy, only the upper half of the specimen is modelled (Figure 7 a)). Details about the element size will be given later. The force-diameter reduction curve is used as target for the optimization procedure and the model parameters are adjusted until a satisfactory agreement between the experimental data and the numerical simulation is found.

The global response obtained in the numerical analysis is compared to the experimental one in Figure 7 b) for the calibrated work-hardening parameters. In addition, Figure 7 b) shows the equivalent plastic strain p developed in the centre of the specimen during the simulation and its value at failure (indicated by the critical diameter ϕ_c). At failure, the equivalent plastic strain reads approximately $p = 1.6$, which we will refer to as the failure strain ε_f in the following. This quantity will later be used when we calibrate both the strain localization and coalescence analyses. The obtained yield stress and work-hardening parameters are given in Table 1, along with the elasticity parameters.

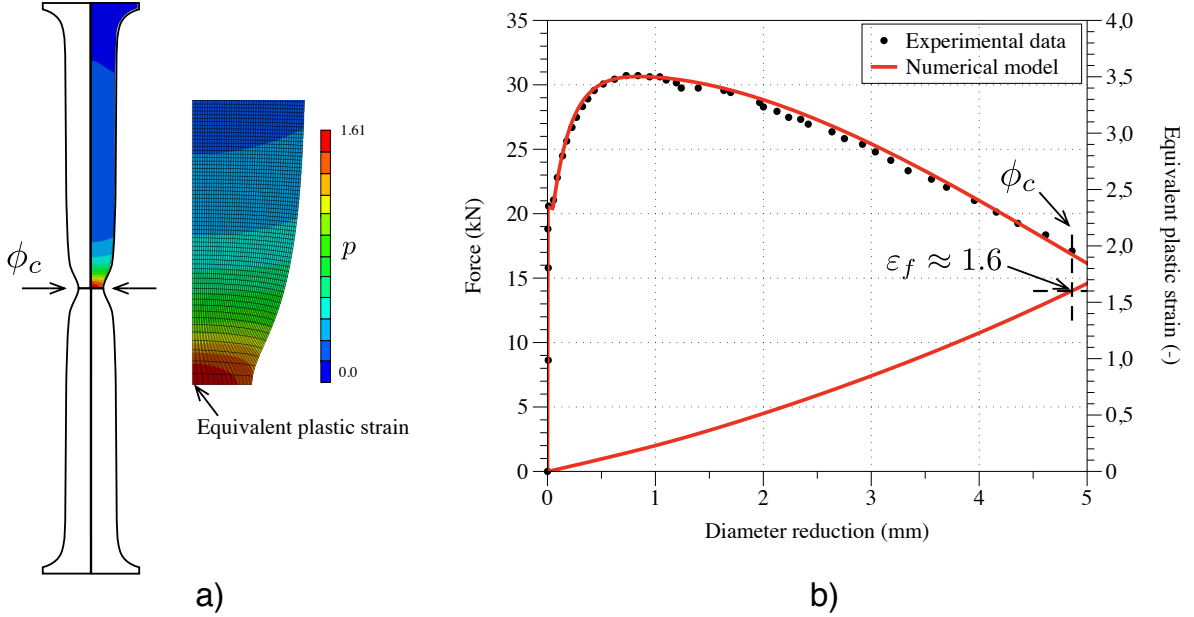


Figure 7: Uniaxial tension test: a) illustration of the finite element mesh after diffuse necking, b) results from simulations with the calibrated metal plasticity model.

4.2. Porous plasticity

The porous plasticity model described in Section 2.4 is an ingredient of the strain localization analyses and we must ensure to calibrate its parameters appropriately and to assess its predictive capabilities. At this stage, the calibration of the porous plasticity model amounts to determine the heuristic correction parameters q_1, q_2, q_3 introduced by Tvergaard (1981), while the initial void volume fraction f_0 and the void nucleation rate A_n are calibrated based on localization analyses. We conduct unit cell calculations with an assumed initial void content $f_0 = 0.001$ under proportional loading to optimize the q_1 and q_2 parameters of the porous plasticity model (see Box 4). To this end, we impose four different stress triaxiality levels to the unit cell ($T = 0.8, 1.0, 1.5,$ and 2.0). We further assume that q_3 and q_1 are linked through $q_3 = q_1^2$, in accordance with Tvergaard (1981). This range of stress triaxiality ratios is deemed representative to typical stress states experienced in the different material tests reported by Basu and Benzerga (2015). The parameter optimization is carried out using the software package LS-OPT (2018) and the optimization scheme used in this study is similar to the one applied by Dæhli et al. (2017). The optimization algorithm is based on minimizing the mean-square error between the unit cell simulations and the porous plasticity model for all the imposed stress states. Both the von Mises equivalent stress and the void volume fraction as function of the equivalent strain are used in the cost function of the optimization algorithm. Since the employed porous plasticity model does

not incorporate any type of accelerated void growth or coalescence model, we chose to truncate the unit cell response curves after the onset of softening (● in Figure 4). The parameters found from the optimization procedure are listed in Table 1.

Table 1: Material parameters of the metal plasticity model and the porous plasticity model.

Elasticity		Porous plasticity				
E [GPa]	ν	q_1	q_2			
210	0.3	1.078	0.985			
Metal plasticity						
σ_0 [MPa]	Q_1 [MPa]	θ_1 [MPa]	Q_2 [MPa]	θ_2 [MPa]	Q_3 [MPa]	θ_3 [MPa]
310.0	127.8	3818.7	200.0	679.2	728.8	168.0

Figure 8 shows results from simulations with the calibrated porous plasticity model compared to the unit cell analyses. The equivalent stress normalized by the yield stress σ_0 and the void volume fraction f normalized by its initial value f_0 (or the normalized porosity f/f_0) are plotted against the equivalent strain up to the onset of necking in Figure 8 a). The equivalent stress and strain measures are respectively defined by σ_{eq} and p in the porous plasticity model (cf. Box 4) and by Σ_{eq} and E_{eq} in the unit cell analyses (cf. Box 1). Under proportional loading and negligible elastic strains, the two equivalent strain measures p and E_{eq} are comparable, but this is not generally valid for arbitrary loading conditions. In the present study, it was checked that the use of total strains in the equivalent strain calculation for the unit cell had negligible influence on the resulting values. The results obtained with the Gurson model, although admittedly not perfect, are deemed satisfactory considering the underlying assumptions and idealizations of the model (Gurson, 1977). In the investigated range of stress triaxiality ratios, we find a marked influence of deformation-induced void shape changes on the stress level and the evolution of the void volume fraction. As the Gurson model assumes spherical void growth, the optimized parameters only produce an average representation of the unit cell analyses. At moderate stress triaxiality ($T = 0.8$), the porous plasticity model overestimates the void growth rate compared to the unit cell analyses, while at higher stress triaxiality ratios ($T = 1, 1.5$) the porous plasticity model underestimates the void growth. At even higher stress triaxiality ($T = 2$), the predictions of the porous plasticity model become rather accurate, which is related to the nearly spherical void evolution in the unit cell calculations and that the Tvergaard parameters q_i are approximately equal to unity, as in the original Gurson model. To indicate the limitations in the predictive capability, Figure 8 b) shows a comparison between the porous plasticity model and the unit cell analyses including data points beyond onset of void coalescence. Since we have not accounted for accelerated void growth due to void coalescence, the porous plasticity model underestimates the void volume fraction with the effect of overestimating the stress level. Figure 8 c) shows the equivalent stress at the onset of material softening (peak stress) normalized by the initial yield stress of the matrix material as function of the stress triaxiality T . A similar curve for the equivalent strain at which the onset of softening occurs is shown in Figure 8 d). From these two figures, we readily infer that the stress and strain levels at the onset of material softening are fairly well represented by the porous plasticity model; in particular for high stress triaxiality ratios.

As stated in the beginning of this section, we must ascertain that the calibrated porous plasticity model yields reliable predictions of the material response, which is assumed to be reflected by the unit cell analyses at the microscopic scale. To this end, we employ two different series of unit cell calculations. More detailed results of this benchmarking are given in Appendix A, while the main conclusions are summarized next.

The first aspect to be verified, is that the calibration of the q_i parameters is independent of the initial

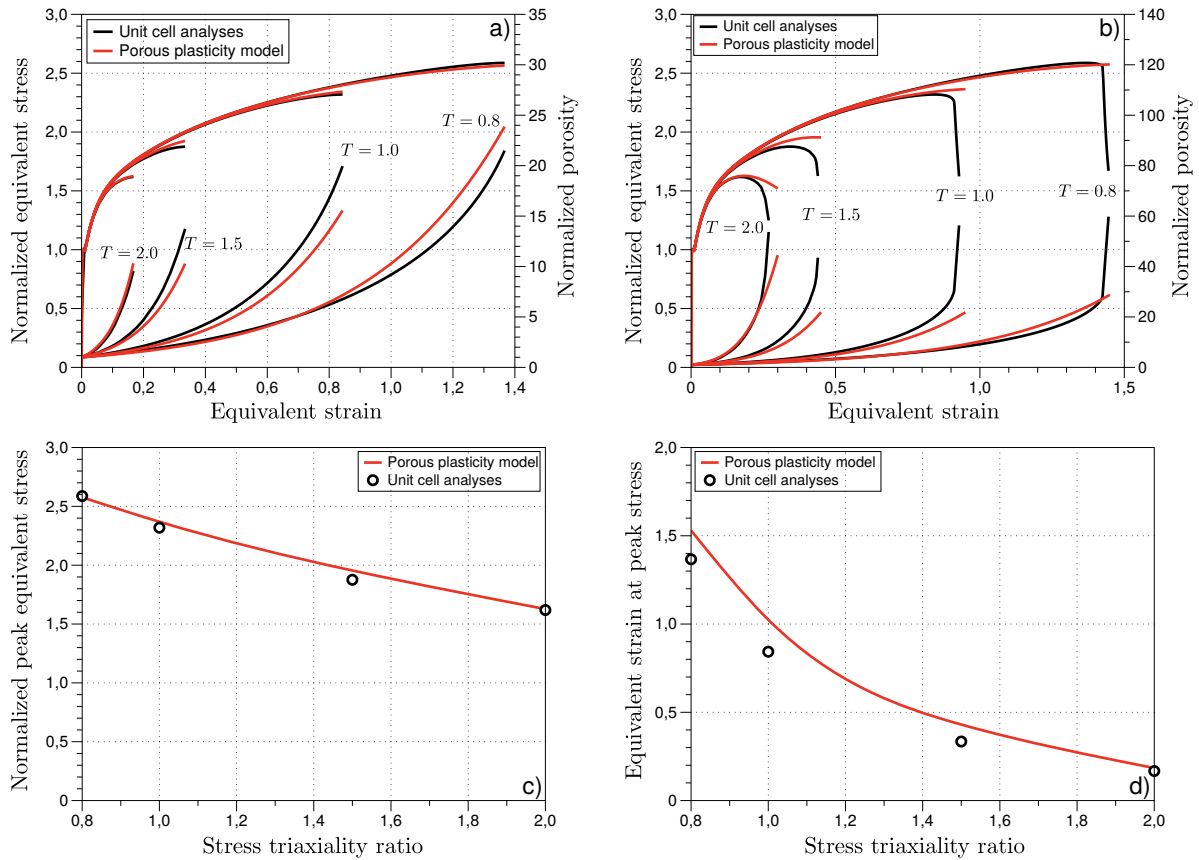


Figure 8: Comparison of the calibrated porous plasticity model with unit cell simulations: equivalent stress and void volume fraction as function of equivalent strain up to a) the onset of the softening and b) the coalescence regime; c) equivalent stress and d) equivalent strain at the onset of softening versus stress triaxiality ratio.

void content f_0 . Indeed, as the void volume fraction inside the imperfection band of the strain localization analyses is not known prior to the calibration of the porous plasticity model, we must ensure that these two operations can be executed independently. To examine this, we perform unit cell simulations with different initial void volume fraction ($f_0 = 0.001, 0.002, 0.005, 0.01, 0.02$) at a constant stress triaxiality ($T = 1$) up to the onset of void coalescence. The main conclusion of this benchmark study is that the q_i parameters are only slightly dependent upon the initial void volume fraction. We therefore conclude that the calibration of the q_i parameters and the imperfection size in the strain localization analyses can be carried out independently.

The second aspect we evaluate in this study is the ability of the porous plasticity model to describe strongly non-proportional loading paths. A series of dedicated unit cell analyses is carried out in which pre-straining at low stress triaxiality ($T = 1/3$) was applied up to incipient necking of the matrix material, followed by reloading at different constant stress triaxiality ratios ($T = 0.8, 1.0, 1.5, 2.0$). While the calibrated porous plasticity model gives fairly accurate predictions for monotonic loading (Figure 8), we find less accurate predictions under strongly non-proportional loading. This effect is most likely due to the complex void shape evolution obtained after pre-straining the unit cell, which is not captured by the adopted porous plasticity model. More advanced porous plasticity models, for instance the models proposed by Keralavarma and Benzerga (2010) or Madou and Leblond (2012), might be able to provide a better description of

this phenomenon. However, we do not pursue this further in the current study, but rather note that the porous plasticity model becomes slightly non-conservative in terms of void evolution at high levels of stress triaxiality.

Despite the discrepancies between the porous plasticity model and the unit cell analyses, we assume herein that the obtained parameters ($q_1 = 1.078$ and $q_2 = 0.985$) are representative. We consequently employ these parameters in the strain localization analyses that are conducted in the following.

4.3. Strain localization and coalescence analyses

The imperfection size required for the strain localization analyses and the volume fraction of initial voids or particles required for the coalescence analyses are calibrated from the uniaxial tension test on the virgin material. This procedure is illustrated in Figure 9. In the strain localization analyses, the deformation gradient history $\mathbf{F}(t)$ in the centre of the specimen from the simulation of the uniaxial tension test is imposed to the material outside the imperfection band. The size of the imperfection, in terms of the initial void volume fraction f_0 or the nucleation rate A_n , is iteratively adjusted until localization is predicted for the same strain level as in the experiments. We note that the maximum volume fraction of nucleated voids was arbitrarily fixed to $f_n^{\max} = 0.01$. Even though this parameter is important, we found it to be a secondary effect. Details regarding this issue will be given subsequently.

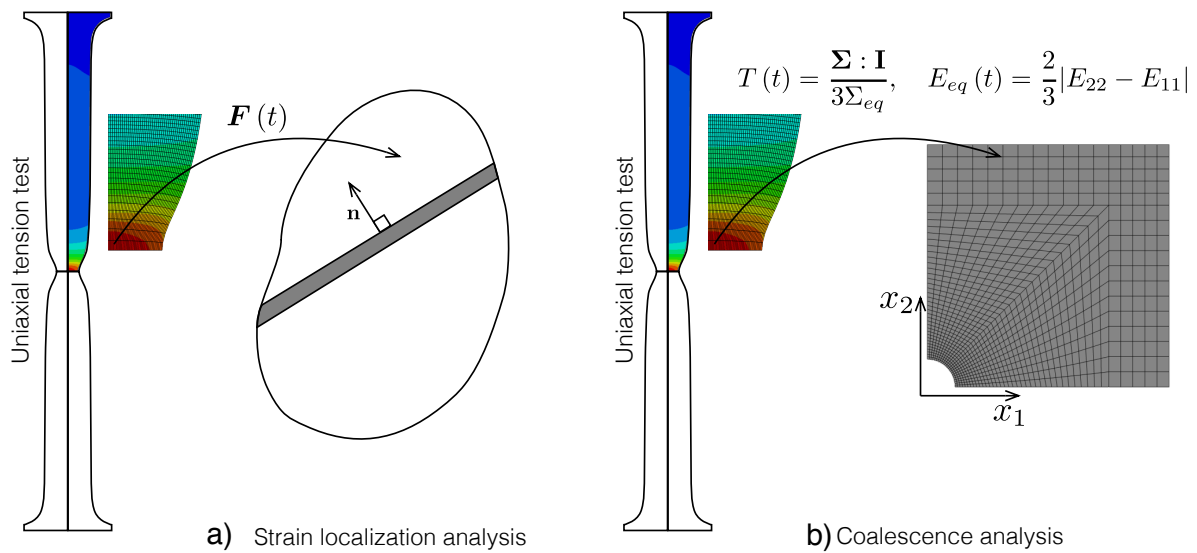


Figure 9: Illustration of the calibration procedure for a) the strain localization analyses and b) the coalescence analyses.

The coalescence analyses are calibrated by imposing the stress triaxiality history from the centre of the tensile test specimen as function of the equivalent strain of the unit cell model. While Dæhli et al. (2016) used a higher-order polynomial function to represent the evolution of the stress triaxiality, we use a tabulated curve that is read by the MPC subroutine in the current work. Linear interpolation of the stress triaxiality data extracted from the simulations of the tensile tests is used to determine the stress triaxiality for arbitrary equivalent strain levels in the unit cell calculations. Considering the large number of increments used in these unit cell simulations (> 100), we consider the error caused by the linear interpolation to be negligible. Similarly to the strain localization analyses, we adjust the volume fraction of initial voids or particles until coalescence occurs at the same strain level as in the test.

The results of this calibration procedure are shown in Figure 10 a) and b) in the case of initial voids or particles, respectively. The blue curves in Figure 10 correspond to the strain localization analyses, whereas the red curves correspond to the coalescence analyses. In the case of initial voids, we observe in Figure 10 a) that the two techniques require a different initial void volume fraction f_0 to obtain the same failure strain. However, their order of magnitude is similar, namely $f_0 = 0.00296$ for the strain localization analyses and $f_0 = 0.00175$ for the coalescence analyses. When we use a particle instead of a void in the coalescence analyses, we find that a slightly lower volume fraction is required to match the experimental failure strain value. As shown in Figure 10 b), a particle volume fraction of $f_p = 0.001$ is required to trigger coalescence at the same overall strain as in the coalescence analyses with an initial void. This difference might be explained by the constraining effect of the particle on the void evolution, which is particularly important at low stress triaxialities. The calibrated parameters are compiled in Table 2.

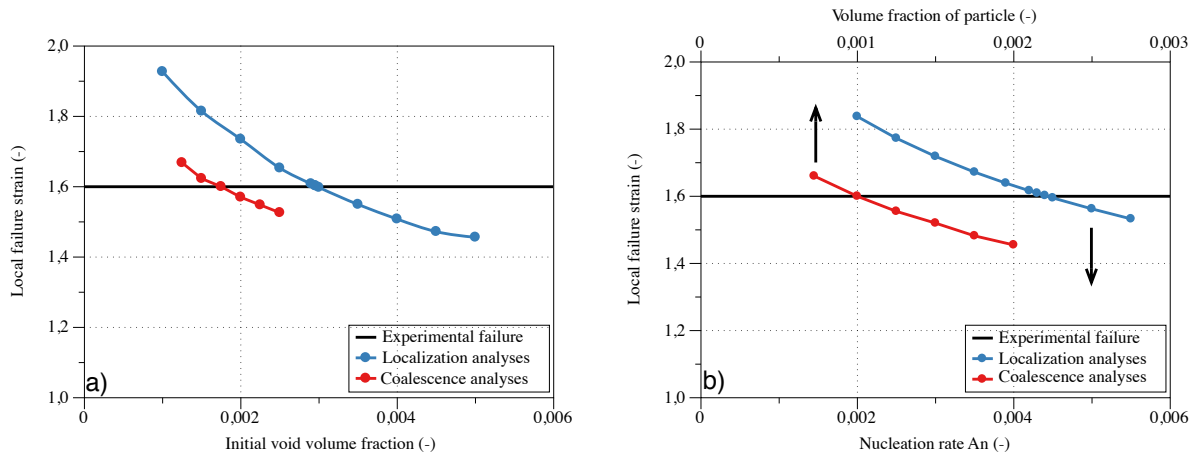


Figure 10: Results of the calibration procedure for the strain localization and coalescence analyses in the case of: a) initial void volume fraction and b) particle/void nucleation.

Figure 11 presents results from the strain localization and coalescence analyses. The von Mises equivalent stress and the void volume fraction are plotted against the equivalent strain for initial voids in Figure 11 a) and for particle/void nucleation in Figure 11 b). In the strain localization analyses, the equivalent plastic strain of the material outside the band (p_0) is chosen, while the global equivalent strain ϵ_{eq} is used for the coalescence analyses. Even though these two quantities are not strictly equal, the difference between them is considered to be negligible under the assumption of small elastic deformations and quasi-proportional loading. The black curves in Figure 11 correspond to the material response outside the band in the strain localization analyses, which is the same as the material response obtained from the simulation of the uniaxial tensile test. We observe in both Figure 11 a) and b) that the strain localization analyses predict a stronger material softening in terms of the von Mises equivalent stress than the coalescence analyses because of the higher void volume fraction that develops in the imperfection band compared to the unit cell analyses. However, close to failure both methods predict a very strong increase in the void volume fraction.

The effect of the maximum volume fraction of nucleated voids f_n^{max} is revealed by the results shown in Figure 11 b). While the continuous blue curve in Figure 11 b) represents the total void volume fraction inside the imperfection band, the dashed blue line corresponds to the volume fraction of nucleated voids (i.e., the time integral of \dot{f}_n in Box 4). The volume fraction of nucleated voids contributes significantly to the total void volume fraction up to an equivalent strain of $p \approx 0.5$. However, void growth dominates from this

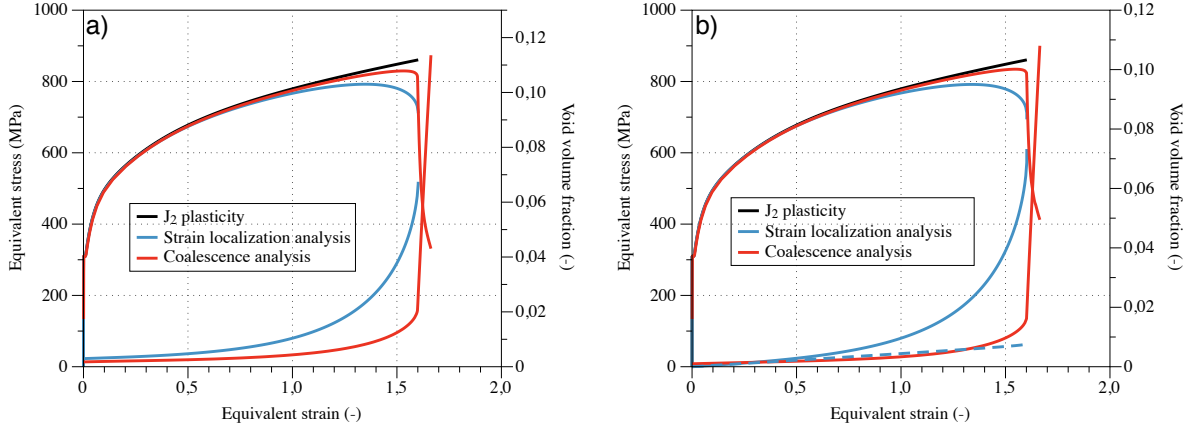


Figure 11: Results from the calibrated strain localization and coalescence analyses for the uniaxial tension test with a) initial void volume fraction and b) particle/void nucleation. The blue dashed line corresponds to the volume fraction of nucleated voids f_n .

strain level and up to localization. At localization, the contribution from void nucleation is roughly 10 % of the total void volume fraction, while the remaining part is linked to void growth. We also observe that the volume fraction of nucleated voids at localization has not reach its upper limit of 1%.

Table 2: Calibrated values of initial void volume fraction f_0 , nucleation rate A_n and particle content f_p used in the strain localization and coalescence analyses.

Localization analyses		Coalescence analyses	
f_0	A_n	f_0	f_p
0.00296	0.0043	0.00175	0.001

5. Numerical results

5.1. Preamble

The aim of this section is to assess the predictive capabilities of the strain localization and coalescence analyses. Since the two methods were calibrated using a single uniaxial tension test, the different notched specimens, either under monotonic or non-monotonic loading, can be used to validate the two approaches. Similarly to the calibration of the two methods in Section 4, we drive the strain localization and coalescence analyses by applying the deformation or stress history from a finite element simulation of the tension test. The deformation gradient history $\mathbf{F}(t)$ extracted from the centre of the various specimens is used to drive the localization analyses, whereas the stress triaxiality at the same location $T(E_{eq})$, given as a function of the equivalent strain, is used to drive the coalescence analyses. As pointed out by Basu and Benzerga (2015), no signs of surface cracking were observed during the various tests, which suggests that failure initiated in the centre of the tensile specimens. Analogously to the work of Morin et al. (2018a), strain localization analyses were conducted across the radius of the tensile specimens to determine where failure would initiate between the centre of the specimen and the notch root. All strain localization analyses predicted localization to occur in the centre of the specimens first and by that confirming the experimental findings of Basu and

Benzerga (2015). Based on this conclusion, all results presented in the next subsections are obtained using the deformation gradient history or stress triaxiality history from the centre of the various notched tensile specimens. We note that the conclusions from the strain localization analyses, with respect to the location of ductile failure initiation, are extrapolated to the coalescence analyses. Due to the axisymmetric unit cell used to predict coalescence, only the information pertaining to the centre of the specimen is relevant in order to respect the symmetries of the unit cell.

Again, the implicit finite element solver ABAQUS/Standard (Dassault Systèmes Simulia, 2014) is used to simulate the notched specimens under both monotonic and non-monotonic loading conditions. The mesh size in the numerical analyses was determined based on the non-monotonic experiments. These specimens, which were pre-deformed under uniaxial tension, are meshed using an average element length of 0.1 mm in the centre of the specimen. Taking into account the pre-straining, we adjusted the mesh size of the uniaxial tension test such that the elements reached the same size as in the simulations of the non-monotonic experiments at the prescribed pre-strain. This resulted in initially biased elements of rectangular shape. The different notched specimens under monotonic loadings are meshed using the same element size and aspect ratio as the simulation model of the uniaxial tensile test. As pointed out by Basu and Benzerga (2015), the numerical simulations of the non-monotonic experiments require a modification in terms of material properties to account for the pre-straining. In the present study, this is done using the initial conditions keyword of ABAQUS, which allows to specify an initial level of equivalent plastic strain for a given set of elements. Deformed configurations of the different notched tensile specimens are given in Figure 12 a) for the monotonic and in Figure 12 b) for the non-monotonic experiments, along with close-up views of the finite element meshes in the vicinity of failure initiation.

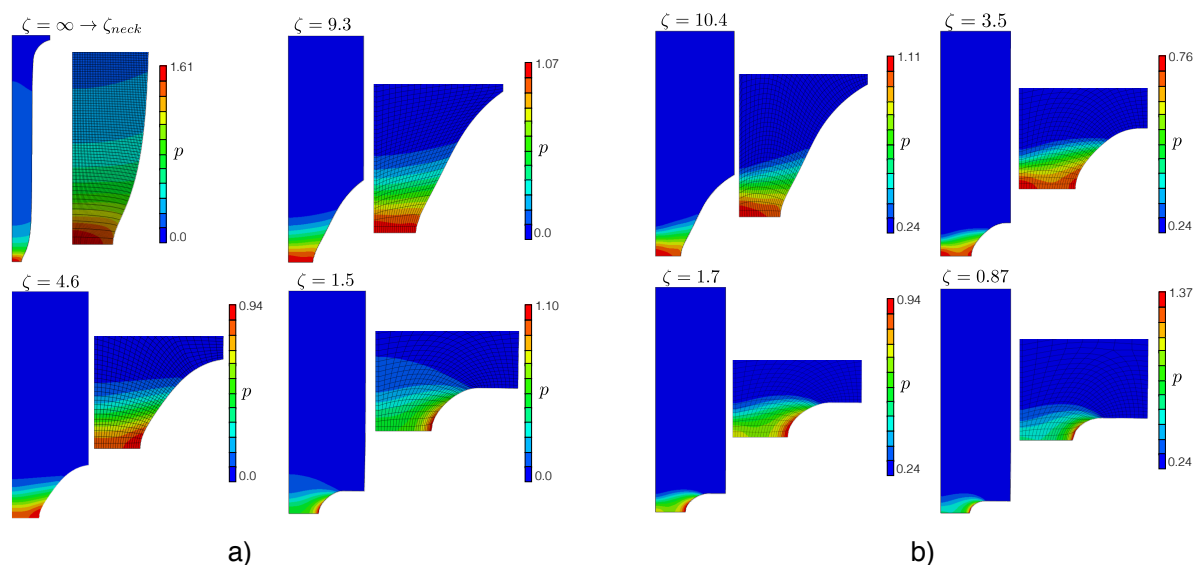


Figure 12: Overview of the deformed specimen geometries and close-up views of the finite element meshes in the vicinity of failure with colour plot of the equivalent plastic strain field: a) the monotonic experiments and b) the non-monotonic experiments.

5.2. Monotonic experiments

The two numerical methods are first applied to the monotonic experiments. Engineering stress-strain curves up to failure are shown in Figure 13 a) and b) for the case of initial void volume fraction and

particle/void nucleation, respectively. The instant of failure initiation reported in Figure 13 is found based on the relationship between the engineering strain and the equivalent strain in the centre of the specimens. Figure 13 a) shows that the coalescence analyses based on an initial void volume fraction provide rather good predictions of the ductility of the tensile specimens, even though the predictions are slightly non-conservative for the specimen with notch acuity $\zeta = 9.3$ and conservative for the one with notch acuity $\zeta = 1.5$. We find good agreement between the localization analyses and the coalescence analyses for the specimens with notch acuity $\zeta = 9.3$ and $\zeta = 4.6$. However, as should be expected, the strain localization analysis yields fairly conservative failure predictions at the highest stress triaxiality, i.e., in the specimen with notch acuity $\zeta = 1.5$ (Figure 13 a)).

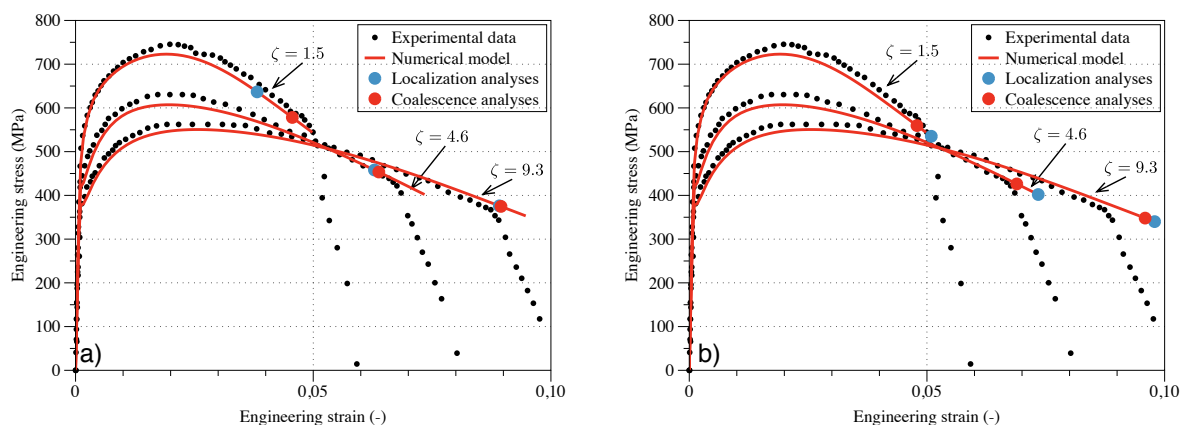


Figure 13: Comparison between the monotonic experiments and the strain localization and coalescence analyses: a) initial void volume fraction and b) particle/void nucleation.

When void nucleation is included inside the imperfection band (Figure 13 b)), we obtain quite accurate predictions for the specimens with notch acuity $\zeta = 1.5$ and $\zeta = 4.6$, while the result is more non-conservative for the specimen with notch acuity $\zeta = 9.3$. The coalescence analyses, in which a particle is included, show better agreement with the experimental data, but again failure is predicted rather late for the specimen with notch acuity $\zeta = 9.3$. A general trend is that the coalescence analyses using a unit cell model with a particle are more conservative than the strain localization analyses with void nucleation. We believe that this is caused by the impingement of the matrix on the particle surface, which is an effect that cannot be captured in the porous plasticity model. In broad terms, the results presented in Figure 13 a) and b) indicate that both the strain localization analyses and the coalescence analyses are able to provide reliable ductility predictions for the investigated material under monotonic and moderately non-proportional loading conditions. The imperfection band approach, though being based on a simplified model, is able to provide reasonable estimates of the ductility.

5.3. Non-monotonic experiments

The results of the strain localization and coalescence analyses applied to the non-monotonic experiments are presented in Figure 14 a) and b) for the case of initial void volume fraction and particle/void nucleation, respectively. In line with the results presented in Figure 13 a), the strain localization analyses with initial void volume fraction f_0 give a fair estimate of the ductility for the specimen with notch acuity $\zeta = 10.4$. However, the results become more conservative when the stress triaxiality increases. We find a good correspondence between the coalescence analyses and the strain localization analyses for the specimen with notch acuity

$\zeta = 10.4$ in Figure 14 a). The coalescence analyses also tend to become more conservative when the stress triaxiality increases, apart from the specimen with notch acuity $\zeta = 0.87$ where the experimental result and the numerical prediction are in good agreement.

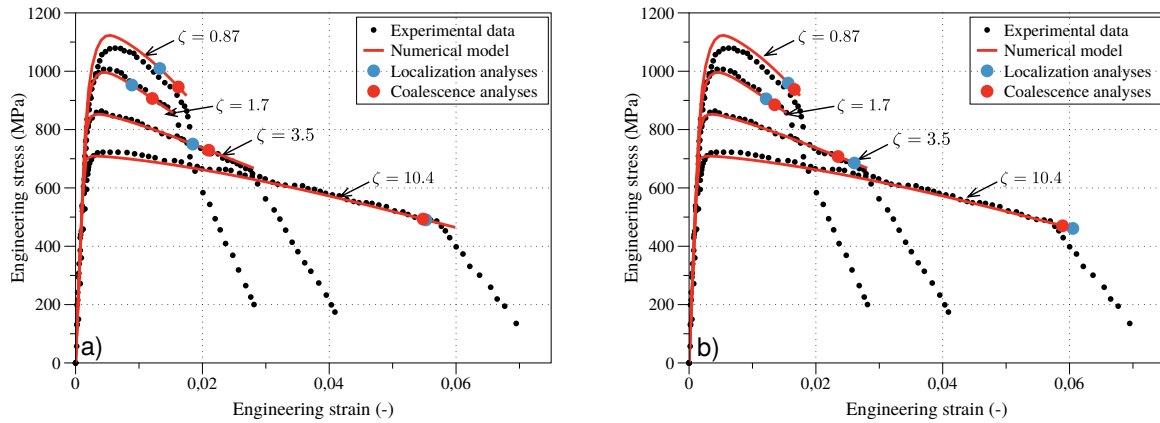


Figure 14: Comparison between the non-monotonic experiments and the strain localization and coalescence analyses: a) initial void volume fraction and b) particle/void nucleation.

When a particle is included in the coalescence analyses (Figure 14 b)), the predictions become rather accurate; however, a somewhat conservative result is obtained for the specimen with notch acuity $\zeta = 3.5$. The strain localization analyses with void nucleation inside the band also exhibit a rather good agreement with the experiments (Figure 14 b)). We find that by changing the imperfection type in the strain localization analyses, the numerical predictions are brought in closer agreement to the coalescence analyses (Figure 14 b)).

The results presented in Figures 13 and 14 suggest that both the coalescence analyses and the strain localization analyses are able to yield quantitative predictions of ductile failure under both moderately and strongly non-proportional loading conditions. While these two techniques are inspired by or based on micromechanical considerations, they both require proper calibration and careful selection of the initial void/particle content or void nucleation parameters to describe the ductility of the material investigated by Basu and Benzerga (2015).

6. Discussion

This section presents a more detailed investigation of the results obtained with the strain localization and coalescence analyses. While the two techniques are based on micromechanical considerations, we do not aim to establish a direct link between the physical process of ductile failure initiation and the process of localization or coalescence represented in the numerical techniques.

6.1. Effect of the imperfection type in strain localization analyses

Based on the results presented in Figures 13 and 14, it appears that the strain localization analyses using either an initial void volume fraction or void nucleation give similar results for moderate levels of stress triaxiality. When the stress triaxiality is increased, the predictions of the strain localization analyses with initial void volume fraction become more conservative compared to the relatively good agreement found with void nucleation (Figures 13 and 14). To explain these trends, we show data pertaining to the material outside

and inside the imperfection band of the strain localization analyses with initial voids or void nucleation in Figure 15. Two tests are considered: the monotonic test with notch acuity $\zeta = 1.5$ in Figure 15 a) and the non-monotonic test with notch acuity $\zeta = 3.5$ in Figure 15 b). The stress triaxiality evolution inside and outside the imperfection band and the evolution of the void volume fraction inside the imperfection band are presented.

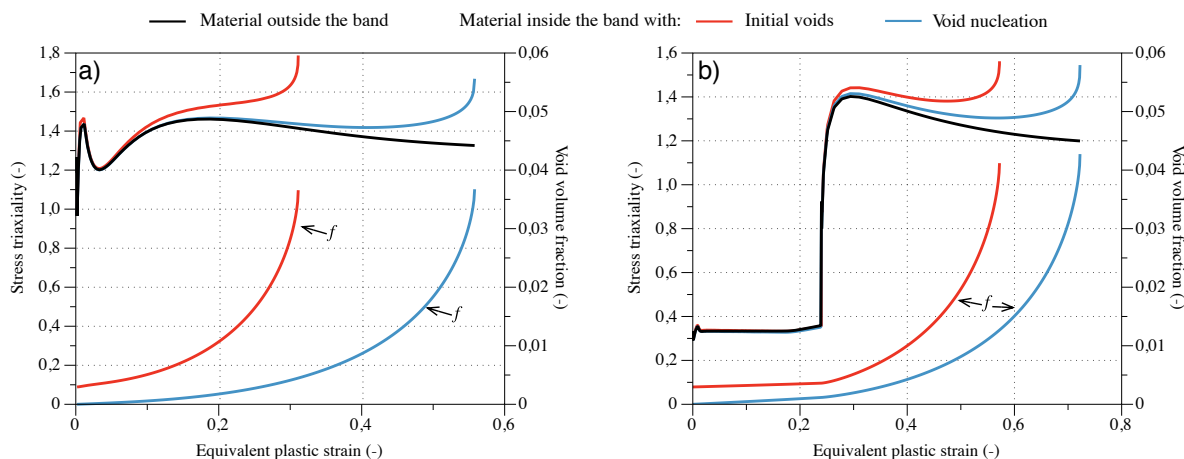


Figure 15: Details of the strain localization analyses: a) the monotonic experiment with notch acuity $\zeta = 1.5$ and b) the non-monotonic experiment with notch acuity $\zeta = 3.5$.

In the case of the monotonic loading (Figure 15 a)), we observe that the stress triaxiality ratio inside the imperfection band deviates substantially from that imposed outside the band. This difference in stress triaxiality is the result of the void volume fraction combined with the compatibility conditions and the continuing equilibrium equations. As the void volume fraction increases, the stress triaxiality inside the imperfection band increases significantly compared to that outside, which accelerates the void growth within the band. As shown in both Figure 15 a) and b), when void nucleation is assumed instead of an initial void volume fraction, the deformation at which the stress triaxiality increases inside the imperfection band is delayed.

6.2. Effect of a particle in coalescence analyses

By comparing the predictions of the coalescence analyses with an initial void or a particle in Figure 14 a) and b), it seems that the presence of a particle in the coalescence analyses is beneficial. This is presumably related to the constraining effect of the particle on the void evolution and that the calibrated particle content f_p is lower than the calibrated initial void volume fraction f_0 . The result is that void coalescence is delayed for the various notched specimens, and particularly for the highest stress triaxiality levels obtained in the specimens with lowest notch acuity. As indicated in Section 4, f_p was found to be 0.1% to predict the same ductility as the coalescence analysis with an initial void volume fraction f_0 of 0.175%.

In addition to the volume fraction of voids/particles, the initial shape of the void resulting from the pre-straining of the unit cell will also influence the onset of void coalescence. To shed some light on this matter, the initial void shape and equivalent plastic strain distribution (p) in the matrix for the coalescence analyses are illustrated in Figure 16. The presence of a particle during the pre-straining phase of the non-monotonic experiments has only minor influence on the residual equivalent plastic strain field of the matrix material. As shown in Figure 16 a), the particle disturbs the equivalent plastic strain field due to the contact with the

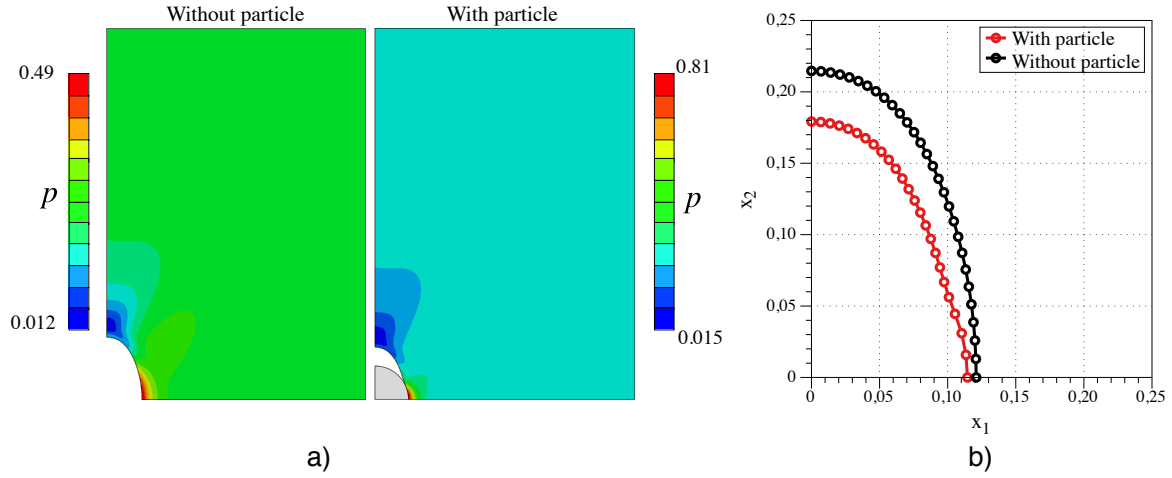


Figure 16: Pre-straining of the unit cell in the coalescence analyses with and without a particle: a) residual equivalent plastic strain fields and b) void size and shapes.

matrix material. In this region, the equivalent plastic strain is slightly higher than in the case of an initial void. However, we note that the equivalent plastic strain distribution is otherwise similar and that the different colours away from the void/particle are due to the different scales; the values of the equivalent plastic strain are very similar ($p \approx 0.24$). Due to the contact on the particle-matrix interface in the unit cell simulation, we observe a slight change in void shape at the end of the pre-straining and thus in the initial stage of the re-loading (Figure 16 b)). Due to the different initial volume fractions of voids, f_0 , and particles, f_p , required to reach coalescence at the desired strain level in the uniaxial tension test, the void volume fraction is different at the end of the pre-straining phase in the two coalescence analyses (Figure 16 b)). While the shape of the voids plays an important role in the ductile failure process (Zhang and Skallerud, 2010; Keralavarma et al., 2011), the difference in void volume fraction appears to be more decisive for the results obtained in the present study.

6.3. Comparison between strain localization and coalescence analyses

Based on the good agreement between the strain localization analyses with void nucleation and the coalescence analyses with a particle (see Figure 13 b) and Figure 14 b)), the evolution of the void volume fraction in these analyses are compared in Figure 17 a) for the monotonic tests and Figure 17 b) for the non-monotonic tests. The results from the uniaxial tension test that were used for the calibration are inserted in Figure 17 a) for reference. Strain localization and coalescence are predicted at very similar strain levels (indicated by filled circles in Figure 17 a) and b)) independently of the deformation mode, i.e., either moderately or strongly non-proportional loading. The evolution of the void volume fraction in the strain localization and coalescence analyses is in some cases very similar, see for instance the non-monotonic test with notch acuity $\zeta = 3.5$ in Figure 17 b), while it is rather different in the case of the monotonic test with notch acuity $\zeta = 9.3$ in Figure 17 a). These differences emerge due to (i) the inaccuracy of the porous plasticity model (presented in Figure 8) and (ii) the different stress triaxiality evolution inside the imperfection band compared to that imposed in the coalescence analyses (Figure 15).

In addition to the strain at which localization or coalescence is predicted, the void content at failure can be investigated. We observe large differences when the specimens are loaded monotonically (Figure 17 a)). While the coalescence analyses predict that the void content at the onset of coalescence increases

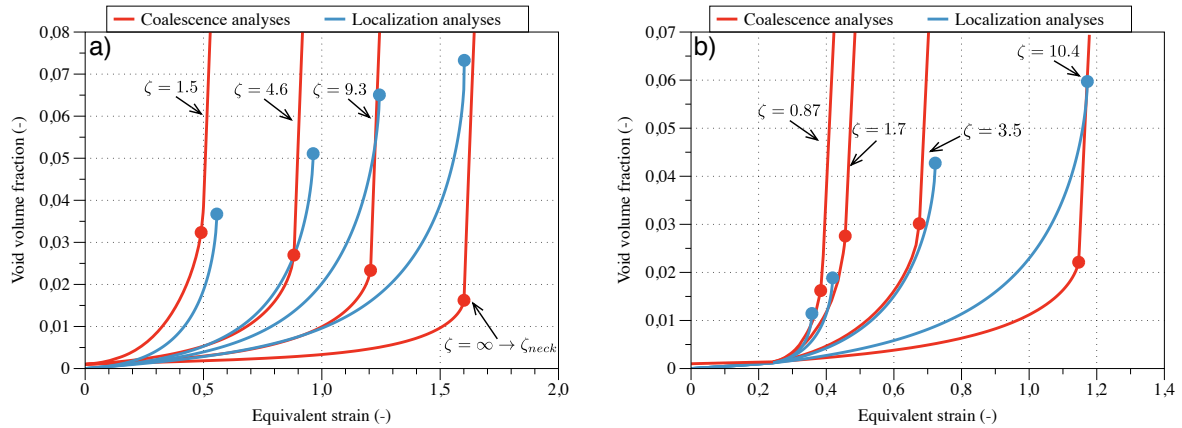


Figure 17: Comparison between the strain localization and coalescence analyses: a) monotonic tests and b) non-monotonic tests.

with increasing stress triaxiality, the strain localization analyses predict that the void content at localization increases when the stress triaxiality decreases. Under non-monotonic loading (Figure 17 b)), the strain localization analyses consistently predict the same trend, while the trend is less clear in the coalescence analyses.

While the onset of coalescence in the unit cell analyses employed in this study is rather well defined, the localization of deformation in the intervoid ligament is quite sensitive to the imposed stress state. This is illustrated in Figure 18 where a unit cell with an initial void volume fraction f_0 of 0.1% is subjected to proportional loading with a constant stress triaxiality ($T = 1$) and constant Lode parameter $L = +1$ or $L = -1$. The results in terms of the von Mises equivalent stress and the void volume fraction as a function of equivalent strain are shown in Figure 18 a), while deformed shapes of the unit cell are shown in Figure 18 b) for the two different Lode parameters. By changing the deformation mode from generalized tension ($L = -1$) to generalized compression ($L = +1$), the unit cell analyses exhibit very similar evolution of the void volume fraction and the equivalent stress up to the point of maximum stress (indicated by filled circles in Figure 18). We note that at this level of stress triaxiality, the Lode parameter only has a small effect on the void growth prior to the onset of material softening. After the peak stress is reached, the response curves for generalized tension and compression diverge, which entails a greater influence of the Lode parameter. Using the shift to a uniaxial straining mode as the coalescence criterion (indicated by a filled square in Figure 18 a)), we find that onset of coalescence is clearly detectable under generalized tension but is not detectable under general compression. The deformed shapes of the unit cells under generalized tension and compression are shown in Figure 18 b) along with field plots of the equivalent plastic strain rate (\dot{p}) in the matrix material. The two deformed shapes are plotted at the same global equivalent strain, which corresponds to the onset of coalescence in generalized tension. In the case of generalized tension, we observe that the deformation localizes in the intervoid ligament, while plastic flow still takes place everywhere in the matrix in generalized compression. Subsequent to this deformation state, the void continues to grow in generalized compression with plastic flow taking place in the entire matrix material until the void impinges on the unit cell edges. Since no instability occurs under generalized compression, this coalescence criterion is unsuitable in the general case. This issue was also addressed by Dæhli et al. (2017).

While it is difficult to define coalescence in the unit cell analyses under generalized compression, the strain localization analyses predict localization also under these stress states. Figure 19 shows the results

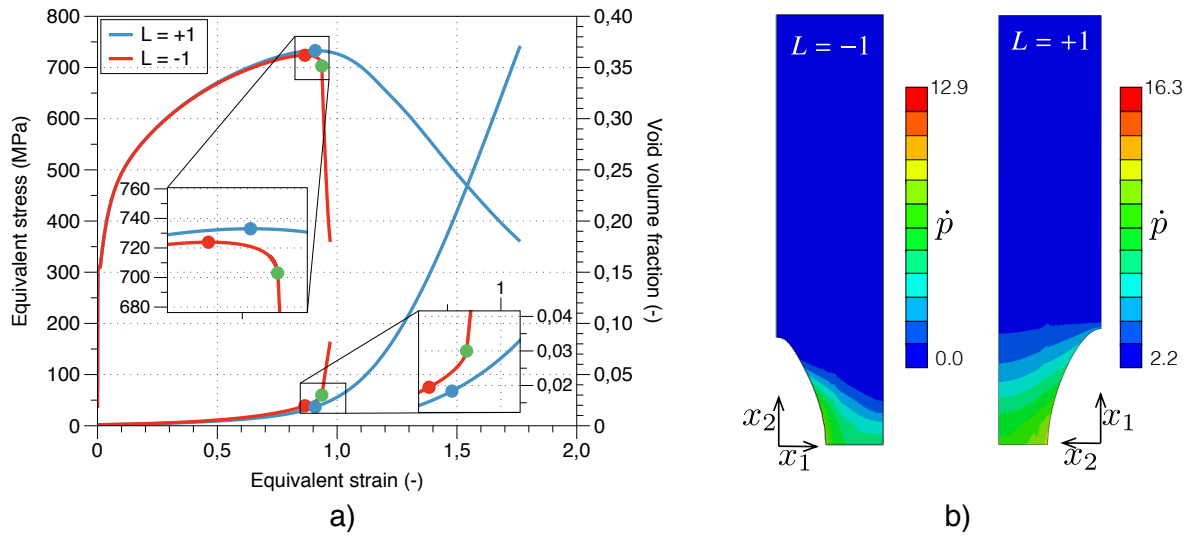


Figure 18: Results from two unit cell analyses with stress triaxiality $T = 1$ and Lode parameter $L = -1$ and $L = +1$, respectively: a) equivalent stress and void volume fraction versus equivalent strain and b) deformed shape of the unit cell with colour plots of the equivalent plastic strain rate field.

of two strain localization analyses performed under constant stress triaxiality ($T = 1$) and constant Lode parameter ($L = -1$ or $L = +1$). In these analyses, the imperfection band is given an initial void volume fraction equal to $f_0 = 0.001$. From these results, we find that localization is predicted under both generalized tension (as already shown) and generalized compression. Similarly to the coalescence analyses, the strain localization analyses predict higher ductility under generalized compression than generalized tension.

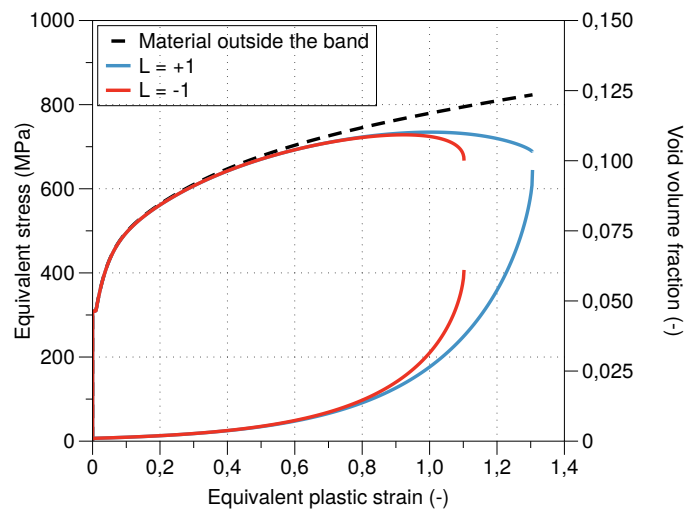


Figure 19: Results of two strain localization analyses with constant stress triaxiality $T = 1$ and Lode parameter $L = -1$ and $L = +1$, respectively.

7. Concluding remarks

We have examined the capabilities of strain localization and coalescence analyses to predict ductile failure initiation under moderately and strongly non-proportional loading conditions. The recent experimental data reported by Basu and Benzerga (2015) were used to calibrate and evaluate the two approaches.

By assuming that ductile failure initiation coincides with strain localization, the imperfection band approach proposed by Rice (1976) is used to predict incipient ductile failure. The material behaviour outside and inside the imperfection band is determined based on a single tensile test. While metal plasticity is assumed outside the imperfection band, the imperfection band itself is governed by the Gurson model (Gurson, 1977) with the heuristic modification of Tvergaard (1981) and two different types of voiding mechanisms: initial void volume fraction or uniform void nucleation. The strain localization analyses are driven using the deformation gradient history extracted from the numerical simulations of the experimental tests. The uniform nucleation rule proves to be beneficial and good agreement is found between the predicted ductility and the experimental data reported by Basu and Benzerga (2015).

Another way to describe the initiation of ductile failure is to consider the onset of coalescence between neighbouring voids. In this study, we used axisymmetric unit cell analyses to study coalescence. By subjecting the unit cells to the stress history obtained in the numerical simulations of the experimental tests, coalescence analyses are used to predict the initiation of ductile failure. As for the strain localization analyses, the behaviour of the matrix material and the void/particle content are determined based on a single tensile test. We found that including a particle in the unit cell is beneficial to predict the ductility of the material investigated by Basu and Benzerga (2015). This approach, employed previously by Dæhli et al. (2016), appears to be capable of predicting the initiation of ductile failure with good accuracy.

The strain localization analyses with uniform nucleation give similar results to the coalescence analyses with a particle. Both methods are able to predict ductile failure under moderately and strongly non-proportional loading paths with reasonable accuracy when they are properly calibrated to experimental data from a single tensile test. While the coalescence analyses based on unit cells are in slightly better agreement to the experiments, the localization analyses require an order of magnitude less computation time and are thus well suited for application in design of structures against failure.

8. Acknowledgements

The authors gratefully appreciate the financial support from NTNU and the Research Council of Norway through the Centre for Advanced Structural Analysis, Project No. 237885 (CASA) and the FRINATEK Programme, Project No. 250553 (FractAl).

Appendix A.

This section is dedicated to the validation of the porous plasticity model used in the strain localization analyses to model the imperfection band. As stated in Section 4, two aspects of the porous plasticity model are considered; (i) the effect of the void content on the q_i parameters introduced by Tvergaard (1981) and (ii) the capacity of the calibrated model to describe strongly non-proportional loading paths.

To evaluate the effect of the initial void volume fraction f_0 on the predictive capabilities of the calibrated porous plasticity model, a series of unit cell analyses with various initial void volume fraction is conducted. To limit the number of numerical analyses, all unit cells are subjected to a constant stress triaxiality of $T = 1$ and a constant Lode parameter of $L = -1$ (generalized tension state). Initial void volume fractions ranging from $f_0 = 0.001$ to $f_0 = 0.02$ are considered in the following. Figure A.1 shows the results from the unit

cell analyses along with the predictions of the porous plasticity model. As a reminder, the porous plasticity model was calibrated using the unit cell analyses described in Section 4 where an initial void volume fraction $f_0 = 0.001$ was used. The results of the porous plasticity model are obtained by simply changing the initial void volume fraction f_0 to match the corresponding unit cell analysis. The normalized equivalent stress (σ_{eq}/σ_0 or Σ_{eq}/σ_0) and the normalized void volume fraction (or normalized porosity f/f_0) as a function of equivalent strain (p or E_{eq}) are presented in Figure A.1 a) and b), respectively. Similar quantities to the ones shown in Figure 8 c) and d) are presented in Figure A.1 c) and d), namely the normalized equivalent stress and the equivalent strain at the onset of softening.

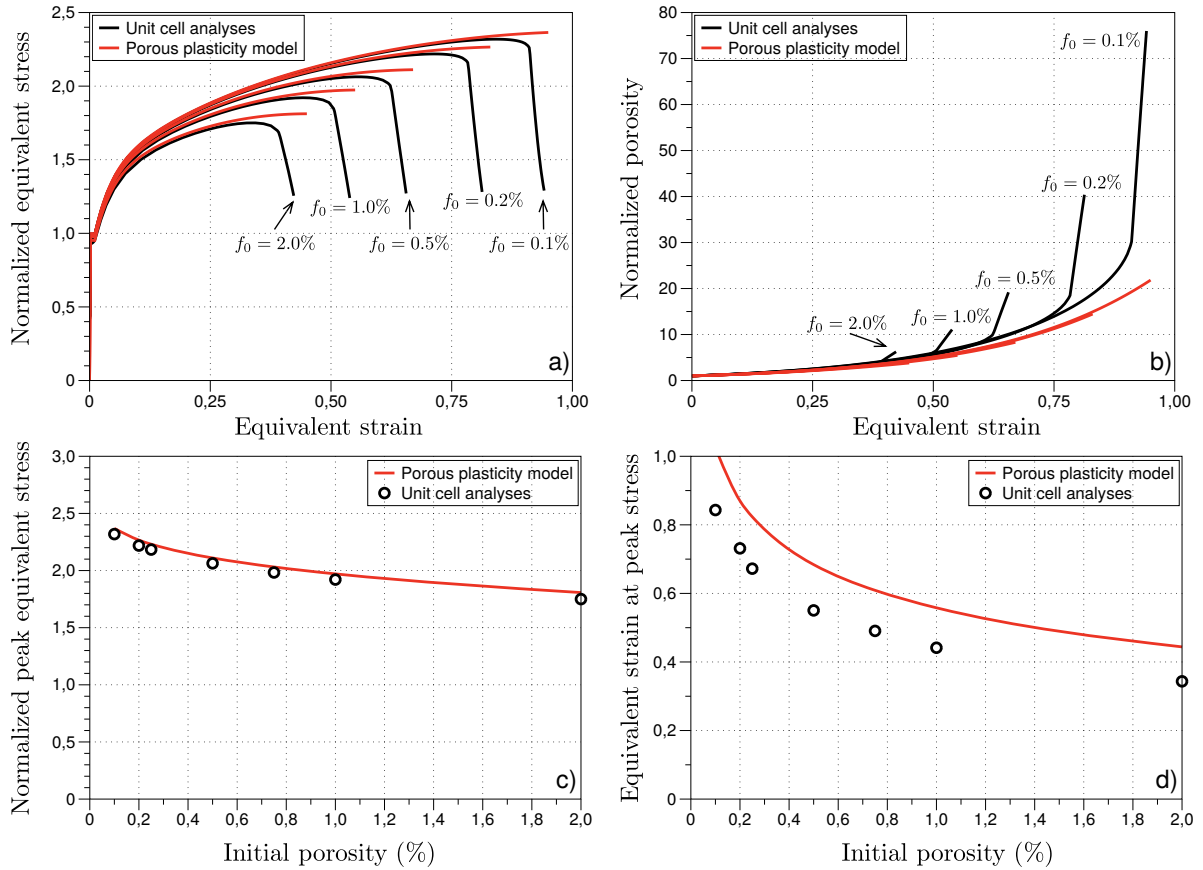


Figure A.1: Effect of the initial void volume fraction f_0 on the predictions obtained by the unit cell analyses and the porous plasticity model.

Based on the comparison shown in Figure A.1 a) and b), we observe that the calibrated porous plasticity model is able to provide a reasonable description of the unit cell analyses up to maximum stress. However, we note that there is a slight dependence of the q_i parameters on the initial void volume fraction f_0 , since the quality of the predictions is slightly deteriorated when the initial void volume fraction is increased. These differences are barely visible when considering the normalized equivalent stress at the onset of softening (Figure A.1 c)), while the onset of softening is predicted later than in the unit cell analyses (Figure A.1 d)). As stated in Section 4, in view of the results presented in Figure A.1, the small dependence of the q_i parameters on the initial void volume fraction is considered negligible, and the calibrations of the q_i parameters and the initial void volume fraction f_0 or void nucleation rate A_n are conducted independently of each other.

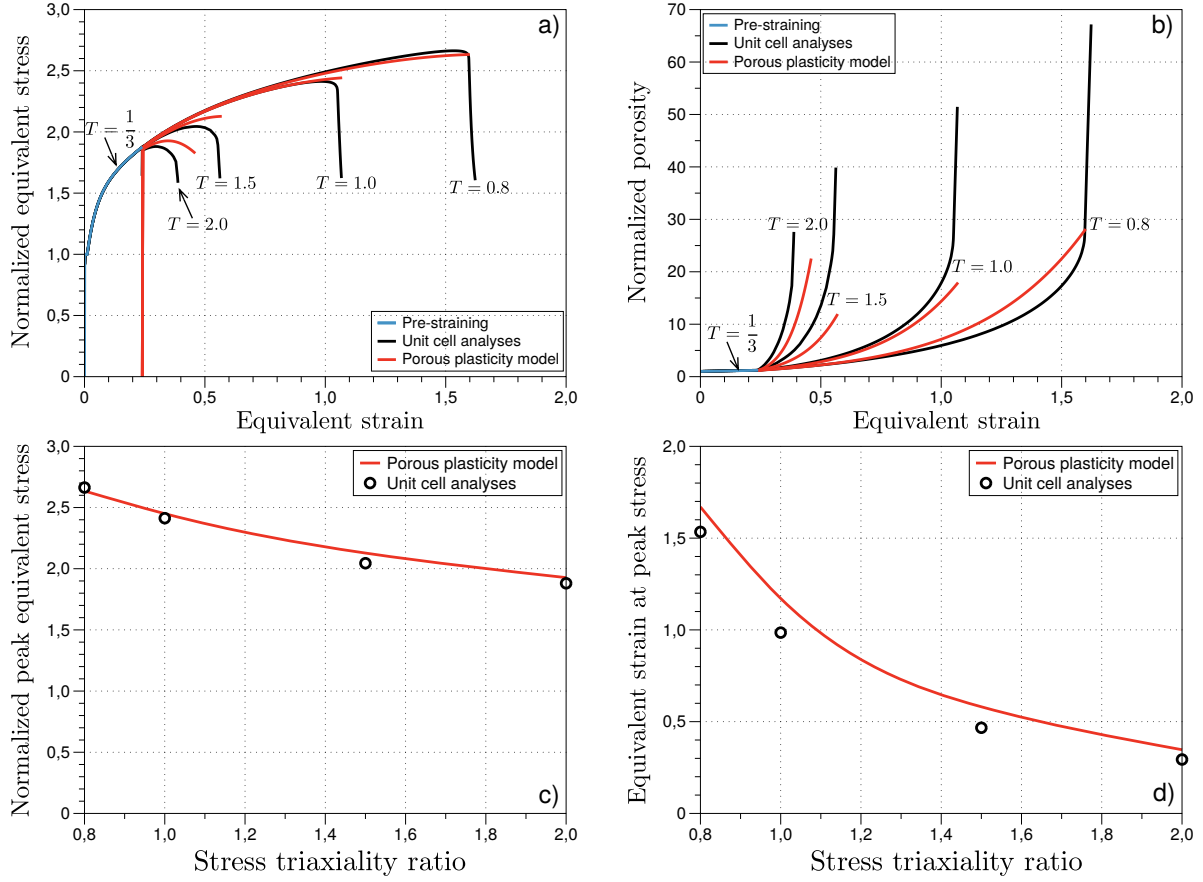


Figure A.2: Effect of a stress triaxiality jump on the predictions obtained by the unit cell analyses and the porous plasticity model.

The second aspect to evaluate is the ability of the porous plasticity model to describe the void growth obtained under strongly non-proportional loading conditions. To this end, unit cell analyses with an initial void volume fraction $f_0 = 0.001$ are subjected to a strongly non-proportional loading, which mimics the non-monotonic experiments of Basu and Benzerga (2015). The unit cell is first subjected to a pre-straining under uniaxial tension ($T = 1/3$) and then unloaded to a stress-free configuration. In the second phase, the pre-deformed unit cells are deformed under constant stress triaxiality until coalescence takes place. Four stress triaxialities are considered here ($T = 0.8, 1.0, 1.5, 2.0$) to cover the range of stress states observed in the experiments. The normalized equivalent stress (σ_{eq}/σ_0 or Σ_{eq}/σ_0) and the normalized void volume fraction (or normalized porosity f/f_0) are presented in Figure A.2 as a function of equivalent strain (p or E_{eq}), whereas the normalized equivalent stress and the equivalent strain at the onset of softening are presented in Figure A.2 c) and d). For moderate stress triaxiality ($T = 0.8, 1.0$) after the pre-straining, we find a good agreement between the predictions obtained by the porous plasticity model and the unit cell analyses. At higher stress triaxiality ($T = 1.5, 2.0$), the predictions of the porous plasticity model are less accurate than in the case of monotonic loading (see Figure 8). These differences are most likely linked to the prolate void shape at the end of the pre-straining (Figure 16). Since the porous plasticity model adopted in this study (Gurson, 1977) is based on spherical voids, the observed trends (Figure A.2) are not captured. To improve

the predictions, more advanced porous plasticity models could be applied (e.g. Madou and Leblond (2012)), but this is considered out of scope of the present study. In view of the inherent limitations of the porous plasticity model, we consider the accuracy obtained for strongly non-proportional loading to be acceptable.

References

- Balan, T., Lemoine, X., Maire, E., Habraken, A. M., 2015. Implementation of a damage evolution law for dual-phase steels in Gurson-type models. *Materials and Design* 88, 1213–1222.
URL <http://dx.doi.org/10.1016/j.matdes.2015.09.075>
- Bao, Y., Wierzbicki, T., 2004. On fracture locus in the equivalent strain and stress triaxiality space. *International Journal of Mechanical Sciences* 46 (1), 81–98.
- Barsoum, I., Faleskog, J., 2007. Rupture mechanisms in combined tension and shear-Experiments. *International Journal of Solids and Structures* 44, 1768–1786.
- Basu, S., Benzerga, A. A., 2015. On the path-dependence of the fracture locus in ductile materials: Experiments. *International Journal of Solids and Structures* 71, 79–90.
URL <http://dx.doi.org/10.1016/j.ijsolstr.2015.06.003><http://linkinghub.elsevier.com/retrieve/pii/S002076831500267X>
- Benzerga, A., Surovik, D., Keralavarma, S., 2012. On the path-dependence of the fracture locus in ductile materials – Analysis. *International Journal of Plasticity* 37, 157–170.
URL <http://dx.doi.org/10.1016/j.ijplas.2012.05.003><http://linkinghub.elsevier.com/retrieve/pii/S0749641912000721>
- Benzerga, A. A., Besson, J., Pineau, A., 2004. Anisotropic ductile fracture: Part I: Experiments. *Acta Materialia* 52 (15), 4623–4638.
- Chen, Y., Clausen, A. H., Hopperstad, O. S., Langseth, M., 2009. Stress-strain behaviour of aluminium alloys at a wide range of strain rates. *International Journal of Solids and Structures* 46 (21), 3825–3835.
URL <http://dx.doi.org/10.1016/j.ijsolstr.2009.07.013>
- Cheng, L., Guo, T., 2007. Void interaction and coalescence in polymeric materials. *International Journal of Solids and Structures* 44 (6), 1787–1808.
- Chu, C. C., Needleman, A., 1980. Void Nucleation Effects in Biaxially Stretched Sheets. *Journal of Engineering Materials and Technology* 102 (3), 249.
URL <http://materialstechnology.asmedigitalcollection.asme.org/article.aspx?articleid=1422824>
- Dæhli, L. E., Morin, D., Børvik, T., Hopperstad, O. S., 2018. A Lode-dependent Gurson model motivated by unit cell analyses. *Engineering Fracture Mechanics* 190, 299–318.
URL <https://doi.org/10.1016/j.engfracmech.2017.12.023>
- Dæhli, L. E. B., Børvik, T., Hopperstad, O. S., 2016. Influence of loading path on ductile fracture of tensile specimens made from aluminium alloys. *International Journal of Solids and Structures* 88-89, 17–34.
URL <http://linkinghub.elsevier.com/retrieve/pii/S0020768316300130>
- Dæhli, L. E. B., Morin, D., Børvik, T., Hopperstad, O. S., 2017. Influence of yield surface curvature on the macroscopic yielding and ductile failure of isotropic porous plastic materials. *Journal of the Mechanics and Physics of Solids* 107, 253–283.
- Dassault Systèmes Simulia, 2014. Abaqus 6.14 CAE User Guide, 1146.
- Erice, B., Roth, C. C., Mohr, D., 2018. Stress-state and strain-rate dependent ductile fracture of dual and complex phase steel. *Mechanics of Materials* 116, 11–32.
URL <http://dx.doi.org/10.1016/j.mechmat.2017.07.020>
- Faleskog, J., Gao, X., Shih, C. F., 1998. Cell model for nonlinear fracture analysis- I- Micromechanics calibration. *International Journal of Fracture* 89 (4), 355–373.
URL <http://www.scopus.com/inward/record.url?eid=2-s2.0-0032273429&partnerID=40&md5=42368241bba9459b16897e5a1575994e><http://link.springer.com/10.1023/A:1007421420901>
- Gruben, G., Fagerholt, E., Hopperstad, O. S., Børvik, T., 2011. Fracture characteristics of a cold-rolled dual-phase steel. *European Journal of Mechanics, A/Solids* 30 (3), 204–218.
URL <http://dx.doi.org/10.1016/j.euromechsol.2011.01.004>
- Gruben, G., Hopperstad, O. S., Børvik, T., 2012. Evaluation of uncoupled ductile fracture criteria for the dual-phase steel Docol 600DL. *International Journal of Mechanical Sciences* 62 (1), 133–146.
URL <http://dx.doi.org/10.1016/j.ijmecsci.2012.06.009>
- Gruben, G., Morin, D., Langseth, M., Hopperstad, O. S., 2017. Strain localization and ductile fracture in advanced high-strength steel sheets. *European Journal of Mechanics, A/Solids* 61, 315–329.
URL <http://dx.doi.org/10.1016/j.euromechsol.2016.09.014>

- Gurson, A. L., 1977. Continuum Theory of Ductile Rupture by Void Nucleation and Growth: Part I – Yield Criteria and Flow Rules for Porous Ductile Media. *Journal of Engineering Materials and Technology* 99 (1), 2–15.
- Haltom, S., Kyriakides, S., Ravi-Chandar, K., may 2013. Ductile failure under combined shear and tension. *International Journal of Solids and Structures* 50 (10), 1507–1522.
URL <http://dx.doi.org/10.1016/j.ijsolstr.2012.12.009><http://linkinghub.elsevier.com/retrieve/pii/S0020768312005203>
- Keralavarma, S. M., Benzerga, A. A., 2010. A constitutive model for plastically anisotropic solids with non-spherical voids. *Journal of the Mechanics and Physics of Solids* 58 (6), 874–901.
URL <http://dx.doi.org/10.1016/j.jmps.2010.03.007>
- Keralavarma, S. M., Hoelscher, S., Benzerga, A. A., 2011. Void growth and coalescence in anisotropic plastic solids. *International Journal of Solids and Structures* 48 (11-12), 1696–1710.
URL <http://dx.doi.org/10.1016/j.ijsolstr.2011.02.020>
- Koplik, J., Needleman, A., 1988. Void growth and coalescence in porous plastic solids. *International Journal of Solids and Structures* 24 (8), 835–853.
- Landron, C., Maire, E., Bouaziz, O., Adrien, J., Lecarme, L., Bareggi, A., 2011. Validation of void growth models using X-ray microtomography characterization of damage in dual phase steels. *Acta Materialia* 59 (20), 7564–7573.
URL <http://dx.doi.org/10.1016/j.actamat.2011.08.046>
- Liao, J., Xue, X., Lee, M. G., Barlat, F., Vincze, G., Pereira, A. B., 2017. Constitutive modeling for path-dependent behavior and its influence on twist springback. *International Journal of Plasticity* 93, 64–88.
- Lou, Y., Yoon, J. W., 2017. Anisotropic ductile fracture criterion based on linear transformation. *International Journal of Plasticity* 93, 3–25.
URL <http://dx.doi.org/10.1016/j.ijplas.2017.04.008>
- LS-OPT, 2018. LS-OPT Support Site.
URL <http://www.lsoptsupport.com/>
- Madou, K., Leblond, J.-B., 2012. A Gurson-type criterion for porous ductile solids containing arbitrary ellipsoidal voids – I: Limit-analysis of some representative cell. *Journal of the Mechanics and Physics of Solids* 60 (5), 1020–1036.
URL <http://dx.doi.org/10.1016/j.jmps.2012.01.010><http://linkinghub.elsevier.com/retrieve/pii/S0022509611002201>
- Manik, T., Holmedal, B., Hopperstad, O. S., 2015. Strain-path change induced transients in flow stress, work hardening and r-values in aluminum. *International Journal of Plasticity* 69, 1–20.
URL <http://dx.doi.org/10.1016/j.ijplas.2015.01.004>
- Marciniak, Z., Kuczyński, K., 1967. Limit strains in the processes of stretch-forming sheet metal. *International Journal of Mechanical Sciences* 9 (9), 609–620.
URL <http://linkinghub.elsevier.com/retrieve/pii/0020740367900665>
- Mear, M., Hutchinson, J., 1985. Influence of yield surface curvature on flow localization in dilatant plasticity. *Mechanics of Materials* 4 (3-4), 395–407.
URL <http://linkinghub.elsevier.com/retrieve/pii/0167663685900353>
- Morin, D., Fourmeau, M., Børvik, T., Benallal, A., Hopperstad, O. S., 2018a. Anisotropic tensile failure of metals by the strain localization theory: An application to a high-strength aluminium alloy. *European Journal of Mechanics, A/Solids* 69 (7491), 99–112.
URL <https://doi.org/10.1016/j.euromechsol.2017.11.015>
- Morin, D., Hopperstad, O. S., Benallal, A., 2018b. On the description of ductile fracture in metals by the strain localization theory. *International Journal of Fracture* 209 (1), 27–51.
URL <http://link.springer.com/10.1007/s10704-017-0236-9>
- Nahshon, K., Hutchinson, J. W., 2008. Modification of the Gurson Model for shear failure. *European Journal of Mechanics, A/Solids* 27 (1), 1–17.
- Needleman, A., Rice, J., 1978. Limits to ductility set by plastic flow localization. *Mechanics of Sheet Metal Forming*, 237 — 265.
- Needleman, A., Tvergaard, V., 1992. Analyses of Plastic Flow Localization in Metals. *Applied Mechanics Reviews* 45 (3S), S3.
URL <http://appliedmechanicsreviews.asmedigitalcollection.asme.org/article.aspx?articleid=1394557>
- Pan, J., Saje, M., Needleman, A., 1983. Localization of deformation in rate sensitive porous plastic solids. *International Journal of Fracture* 21 (4), 261–278.
- Papasidero, J., Doquet, V., Mohr, D., 2014. Determination of the Effect of Stress State on the Onset of Ductile Fracture Through Tension-Torsion Experiments. *Experimental Mechanics* 54 (2), 137–151.
URL <http://link.springer.com/10.1007/s11340-013-9788-4>
- Papasidero, J., Doquet, V., Mohr, D., 2015. Ductile fracture of aluminum 2024-T351 under proportional and non-proportional multi-axial loading: Bao-Wierzbicki results revisited. *International Journal of Solids and Structures* 69-70, 459–474.

- URL <http://dx.doi.org/10.1016/j.ijsoistr.2015.05.006>
- Pedersen, K. O., Lademo, O. G., Berstad, T., Furu, T., Hopperstad, O. S., 2008. Influence of texture and grain structure on strain localisation and formability for AlMgSi alloys. *Journal of Materials Processing Technology* 200 (1-3), 77–93.
- Rice, J. R., 1976. The localization of plastic deformation. In: *14th International Congress of Theoretical and Applied Mechanics*, pp. 207–220.
- Roth, C. C., Mohr, D., 2014. Effect of strain rate on ductile fracture initiation in advanced high strength steel sheets: Experiments and modeling. *International Journal of Plasticity* 56, 19–44.
URL <http://dx.doi.org/10.1016/j.ijplas.2014.01.003>
- Roth, C. C., Mohr, D., 2015. Ductile fracture experiments with locally proportional loading histories. *International Journal of Plasticity* 79, 328–354.
URL <http://dx.doi.org/10.1016/j.ijplas.2015.08.004>
- Rudnicki, J. W., Rice, J. R., 1975. Conditions for the localization of deformation in pressure-sensitive dilatant materials. *Journal of the Mechanics and Physics of Solids* 23 (6), 371–394.
- Saje, M., Pan, J., Needleman, A., 1982. Void nucleation effects on shear localization in porous plastic solids. *International Journal of Fracture* 19 (3), 163–182.
- Tarigopula, V., Hopperstad, O. S., Langseth, M., Clausen, A. H., 2009. An evaluation of a combined isotropic-kinematic hardening model for representation of complex strain-path changes in dual-phase steel. *European Journal of Mechanics, A/Solids* 28 (4), 792–805.
URL <http://dx.doi.org/10.1016/j.euomechsol.2008.12.004>
- Thomas, N., Basu, S., Benzerga, A. A., 2016. On fracture loci of ductile materials under non-proportional loading. *International Journal of Mechanical Sciences* 117 (1), 135–151.
URL <http://dx.doi.org/10.1016/j.ijmecsci.2016.08.007>
- Tvergaard, V., 1981. Influence of voids on shear band instabilities under plane strain conditions. *International Journal of Fracture* 17 (4), 389–407.
- Vadillo, G., Fernández-Sáez, J., 2009. An analysis of Gurson model with parameters dependent on triaxiality based on unitary cells. *European Journal of Mechanics, A/Solids* 28 (3), 417–427.
URL <http://dx.doi.org/10.1016/j.euomechsol.2008.10.005>
- Vysochinskiy, D., Coudert, T., Hopperstad, O. S., Lademo, O.-G., Reyes, A., 2018. Experimental study on the formability of AA6016 sheets pre-strained by rolling. *International Journal of Material Forming* (11), 541–557.
URL <http://link.springer.com/10.1007/s12289-017-1363-6>
- Wen, W., Borodachenkova, M., Tomé, C. N., Vincze, G., Rauch, E. F., Barlat, F., Grácio, J. J., 2015. Mechanical behavior of Mg subjected to strain path changes: Experiments and modeling. *International Journal of Plasticity* 73, 171–183.
URL <http://dx.doi.org/10.1016/j.ijplas.2014.10.009>
- Westermann, I., Pedersen, K. O., Furu, T., Børvik, T., Hopperstad, O. S., 2014. Effects of particles and solutes on strength, work-hardening and ductile fracture of aluminium alloys. *Mechanics of Materials* 79, 58–72.
URL <http://dx.doi.org/10.1016/j.mechmat.2014.08.006>
- Xue, Z., Faleskog, J., Hutchinson, J. W., 2013. Tension-torsion fracture experiments - Part II: Simulations with the extended Gurson model and a ductile fracture criterion based on plastic strain. *International Journal of Solids and Structures* 50 (25-26), 4258–4269.
URL <http://dx.doi.org/10.1016/j.ijsoistr.2013.08.028>
- Xue, Z., Pontin, M. G., Zok, F. W., Hutchinson, J. W., 2010. Calibration procedures for a computational model of ductile fracture. *Engineering Fracture Mechanics* 77 (3), 492–509.
URL <http://dx.doi.org/10.1016/j.engfracmech.2009.10.007>
- Yamamoto, H., 1978. Conditions for shear localization in the ductile fracture of void-containing materials. *International Journal of Fracture* 14 (4), 347–365.
- Yu, H., Olsen, J. S., He, J., Zhang, Z., 2016. Effects of loading path on the fracture loci in a 3D space. *Engineering Fracture Mechanics* 151, 22–36.
URL <http://dx.doi.org/10.1016/j.engfracmech.2015.11.005>
- Zhang, Z. L., Skallerud, B., 2010. Void coalescence with and without prestrain history. *International Journal of Damage Mechanics* 19 (2), 153–174.